Mechanisms of Heat Flux Across the Southern Greenland Continental Shelf in 1/10° and 1/12° Ocean/Sea Ice Simulations

Theresa J. Morrison[1] [ID], **Dmitry S. Dukhovskoy[2,3]** [ID], **Julie L. McClean[1]** [ID], **Sarah T. Gille[1]** [ID], and **Eric P. Chassignet[2]** [ID]

[1]Scripps Institution of Oceanography, University of California San Diego, La Jolla, CA, USA, [2]Center for Ocean-Atmospheric Prediction Studies, Florida State University, Tallahassee, FL, USA, [3]Environmental Modeling Center, The National Centers for Environmental Prediction, National Weather Service, National Oceanic and Atmospheric Administration, College Park, MD, USA

Abstract The presence of warm Atlantic water on the Greenland continental shelf has been connected to the accelerated melting of the Greenland Ice Sheet, particularly in the southwest and southeast shelf regions. Results from two high-resolution coupled ocean-sea ice simulations that utilized either the 1/10° Parallel Ocean Program (POP) or the 1/12° HYbrid Coordinate Ocean Model (HYCOM) are used to understand the flux of heat on and off the southern Greenland shelf. The analysis reveals that the region of greatest heat flux onto the shelf is southeast Greenland. On the southwestern shelf, heat is mainly exported from the shelf to the interior basins. We identify differences in the shelf break current structure and on-shelf heat content between the two simulations. Just south of the Denmark Strait, there is a seasonally persistent pattern of multi-day variability in the cross-shelf heat flux in both simulations. In the POP simulation, this high-frequency signal results in net on-shore heat flux. In the HYCOM simulation, the signal is weaker and results in net off-shelf heat flux. This variability is consistent with Denmark Strait Overflow eddies traveling along the shelf break.

Plain Language Summary Melting of the Greenland Ice Sheet has been accelerating in recent decades because of rising ocean and air temperatures. Warm ocean water in the deep basin from the subtropical North Atlantic is separated from the ice sheet margin (glacier termini in the Greenland fjords) by the shallower continental shelf region. In this study we compare two simulations of the ocean and sea ice that represent the currents and eddying motions around Greenland realistically. We identify how and where heat is moved on and off the southern Greenland shelf and consider the results to be robust when they are common to both simulations. Warm water mainly moves onto the southeast shelf and off the southwest shelf; the currents on the shelf transport the warm water around the southern tip of Greenland. Near the Denmark Strait we identify oscillations in the warm water crossing onto the shelf that are associated with the presence of Denmark Strait Overflow eddies. On average, these eddies move heat onto the shelf in one model and off the shelf in the other. Understanding how warm water reaches the shelf allows us to better understand how the ocean contributes to the melting of the Greenland Ice Sheet.

1. Introduction

The Greenland Ice Sheet (GIS) is losing mass at an increasing rate, from 51 ± 17 GT yr^{-1} in the 1980s to 286 ± 20 GT yr^{-1} in the 2010s (Mouginot et al., 2019). From 1972 to 2018, this mass loss has contributed 13.7 ± 1.1 mm to global sea level rise (Mouginot et al., 2019). Recently, B. Smith et al. (2020) reported a total mass loss of 200 ± 12 GT yr^{-1} from 2003 to 2019. Projections of sea level rise due to ice sheet mass loss emphasize the short-term (next 100 years) importance of the GIS contribution as oceanic and atmospheric temperatures rise (Meehl et al., 2007). The limited representation of both ice sheet dynamics and ice-sheet connections to the ocean and atmosphere in climate models contributes significantly to the uncertainty of these projections. An estimated 15%–25% of total mass loss from the GIS is from melting marine terminating glaciers, with an additional 15%–25% from calving fluxes (Benn et al., 2017).

The margin of the GIS is comprised of both land-terminating and marine-terminating glaciers. The marine-terminating glaciers are the primary connection between the ocean and the GIS via the circulation in the deep narrow fjords where they are located. Warm salty water, mainly of subtropical North Atlantic origin, is thought to provide the source of heat needed for ocean-driven melting (Rignot et al., 2012; Straneo &
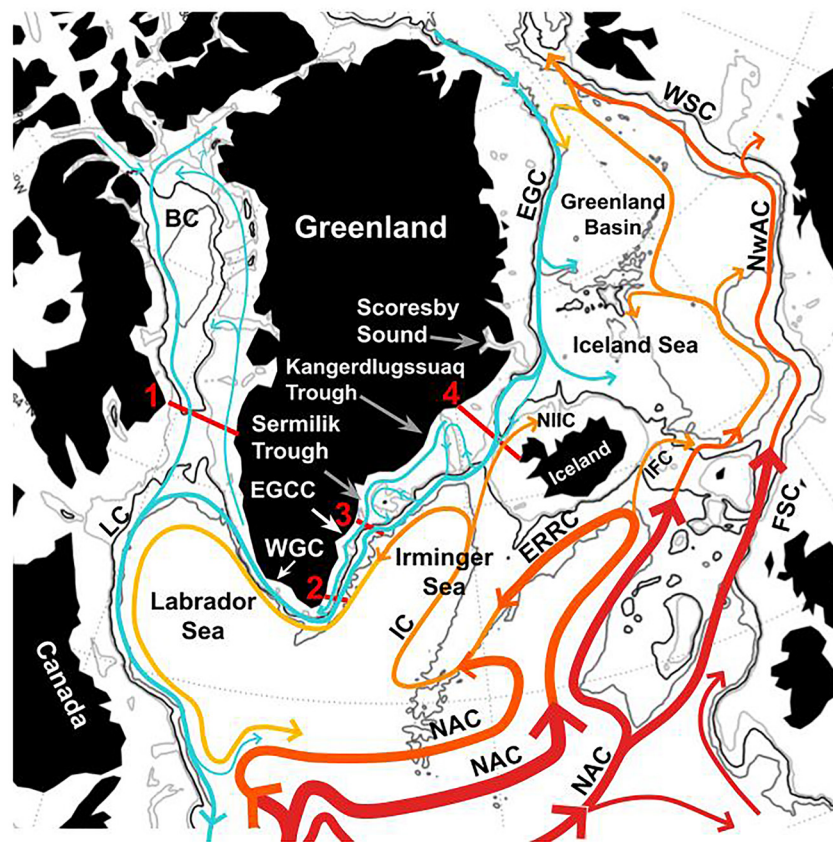
Figure 1. Schematic of circulation in the Subpolar North Atlantic, isobaths are plotted at 400, 800, and 2,000 m. Major currents are labeled: North Atlantic Current (NAC), East Reykjanes Ridge Current (ERRC), Irminger Current (IC), East Greenland Current (EGC), East Greenland Coastal Current (EGCC), West Greenland Current (WGC), Labrador Current (LC), Baffin Current (BC), North Icelandic Irminger Current (NIIC), Iceland-Faroe Current (IFC), Faroe-Shetland Current (FSC), Norwegian Atlantic Current (NwAC), and West Spitsbergen Current (WSC). The major transects used to divide the regions on the shelf are labeled 1–4: (1) Davis Strait, (2) Cape Farewell Gate, (3) Sermilik Gate, (4) Denmark Strait. After Holliday et al. (2018) with additions from (Furevik & Nilsen, 2005; Håvik et al., 2017; Rossby et al., 2018; Saini et al., 2020; Sutherland & Pickart, 2008).

Heimbach, 2013). Marine-terminating glaciers in the southeastern portion of the GIS are particularly vulnerable to ocean-driven melting as they are in closest proximity to the location where Atlantic-originated water intrudes onto the continental shelf (Millan et al., 2018). Over the southeast portion of the GIS, the observed mass loss (Luthcke et al., 2006; Van den Broeke et al., 2009; Wouters et al., 2008) is, in part, attributed to warming ocean conditions (Howat et al., 2008), but it is difficult to separate these effects from those of atmospheric warming (Hanna et al., 2013; Straneo et al., 2013). The presence of warm water on the southwest shelf has also been reported (Straneo et al., 2012; Sutherland et al., 2013). Observations from specific glacial fjords have shown warming of ocean water preceding glacial retreat events (Christoffersen et al., 2012; Holland et al., 2008), implying that in some regions heat from the ocean may be the leading driver of ice sheet mass loss. Within fjords, observations have provided estimates of the penetration of warm water to the front of glaciers (Jackson et al., 2014) given the presence of Atlantic-sourced water on the continental shelf.

The Greenland continental shelf is impacted by the fresh and cold water masses exported from the Arctic Ocean as well as the warm and salty water masses advected from the North Atlantic (Figure 1, redrawn based on Holliday et al. (2018)). Warm water from the subtropical gyre is advected into the subpolar gyre by the North Atlantic Current (NAC), an extension of the Gulf Stream. The NAC consists of multiple northward branches; eastward branches enter the Nordic seas, while those to the west retroflect to enter the Irminger Current (Holliday et al., 2018). Just south of the Denmark Strait, the Irminger Current retroflects, and its primary branch heads southward along the Greenland continental shelf break. On the Greenland continental shelf, from Fram Strait to Cape Farewell, the East Greenland Current (EGC) flows southward, advecting cold fresh water from the Arctic

and seasonal sea ice melt. The weaker and narrower East Greenland Coastal Current (EGCC) is present onshore of the EGC both north and south of the Denmark Strait (Foukal et al., 2020; Håvik et al., 2017; Sutherland & Pickart, 2008).

The transport at the Denmark Strait across the sill has multi-day variability associated with boluses and pulses of overflow water (Appen et al., 2017). Downstream, mesoscale variability is dominated by Denmark Strait Overflow eddies (DSO eddies). These eddies have been studied in observations (Appen et al., 2014; Moritz et al., 2019) and models (Almansi et al., 2017, 2020). Spall and Price (1998) used an idealized model to show that DSO eddies form south of the Denmark Strait as a result of the potential vorticity anomaly associated with the transport of overflow water across the sill. They further showed that these eddies propagate along the shelf break with the phase speed of a topographic Rossby wave (TRW). This model-based result was shown to be consistent with observations of DSO eddies at a mooring array 280 km downstream of the Denmark Strait by Appen et al. (2014).

The role of ocean heat in melting the Greenland Ice Sheet has motivated many studies that focus on how warm water reaches the glacial face. Key questions asked include what mechanisms are responsible for property transport from the shelf into fjords (Fraser & Inall, 2018; Jackson et al., 2014, 2018) or toward the ice sheet within specific troughs (Christoffersen et al., 2011; Gelderloos et al., 2017). Gillard et al. (2020) took a comprehensive approach to studying the heat fluxes into specific troughs in east and west Greenland. They found that the seasonal peak in the heat content of the troughs was linked to the distance from the Irminger Sea, indicating the importance of Irminger Water as a source of heat for west Greenland troughs as well as east Greenland troughs. In comparing simulations with and without storms, they found that without storms there was greater heat flux into the Helheim Glacier trough (located on the Southeast Continental Shelf). The present study expands on the underlying theory of Gillard et al. (2020) by looking not just at specific troughs but the entire southern Greenland continental shelf.

Our study focuses on two mechanisms of cross-shelf heat flux as depicted by two atmospheric forced coupled ocean–sea ice simulations performed with 1/10° and 1/12° configurations of the Parallel Ocean Program (POP) and the HYbrid Coordinate Ocean Model (HYCOM), respectively. By comparing temperature on the shelf and the cross-shelf heat flux in the two simulations, we are able to gain insight into the dominant mechanisms of shelf–basin exchange. The two simulations are configured differently and use different atmospheric forcing and therefore are independent experiments in which the mechanisms that drive on-shelf heat flux and shelf–basin exchange are explored. Robust processes are expected to be found in both simulations.

In Section 2, we begin with a description of the model configurations followed by definitions of the cross-shelf fluxes and the continental shelf control volume. In this section, we also examine the spatial patterns of temperature and cross-shelf heat flux around then entire Greenland continental shelf to motivate our focus on southern Greenland. In Section 2.4, we compare the temperature and velocity from the simulations, with relevant observations included for context. In Section 3, we present the mean heat flux, identify a high-frequency propagating signal, and provide evidence showing it is consistent with DSO eddies. In Section 3.4, we find that the contribution of the high-frequency signal to the cross-shelf heat flux differs between the simulations.

2. Methods

2.1. Model Descriptions

The two coupled ocean–sea ice models that we compare have horizontal resolutions that are comparable to the first baroclinic Rossby radius of deformation (λ_1) in this region (6–8 km in the deep ocean). The effective grid spacing in the study region in POP is ∼5–6 km and ∼4–5 km in HYCOM. Models with this resolution are classified as "eddy-permitting" (Dukhovskoy et al., 2016; Nurser & Bacon, 2014) since their grid spacings are greater than half the size of λ_1 (Hallberg, 2013). The first baroclinic Rossby radius is even smaller on the continental shelf (2–4 km Nurser & Bacon, 2014); therefore, both models have limited ability to capture small (less than ∼10 km) mesoscale shelf processes. Each model is forced by a different set of atmospheric reanalysis, and neither assimilates observations. This allows each model to act as an independent representation of the dynamics in this region. Both models are coupled to the same version of the sea ice model and do not include any representation of freshwater from GIS melt.

2.1.1. 0.1° Global POP—CICE 4

We use results from a global 62-year (1948–2009) simulation of POP version 2 (Dukowicz & Smith, 1994) and the Community Ice Code version 4 (CICE4; Hunke et al., 2010) coupled together in the Community Earth System Model (CESM; Hurrell et al., 2013) version 1.2 framework (McClean et al., 2018). For further details on this simulation, see Wang et al. (2018, 2021); Palóczy et al. (2018, 2020); Castillo-Trujillo et al. (2021); Arzeno-Soltero et al. (2021). This simulation is referred to as POP from here on in the text.

The ocean and sea ice models are on a 0.1° tripolar grid with an effective horizontal resolution of ∼5–6 km in the study region. POP has 42 non-uniformly spaced vertical levels; they range from having 10-m spacing at the surface to 250 m in the deep ocean. The bathymetry is based on ETOPO2 with minor modifications in the Arctic (more details are given by McClean et al. (2011)). Partial bottom cells are used to more smoothly represent the bathymetry. The ocean model has an implicit free surface and is globally volume conserving.

The atmospheric forcing is given by the Coordinated Ocean-ice Reference Experiment–II (CORE-II) corrected interannually varying fluxes (CIAF; Large & Yeager, 2009) and has a horizontal resolution of ∼1.9°. Ocean surface evaporation and precipitation fluxes and runoff are implemented using virtual salt fluxes; for this simulation, a surface salinity restoring condition with an effective timescale of about 4 years limits model drift. POP's ocean properties, potential temperature and salinity, were initialized from the World Hydrographic Program Special Analysis Center climatology (Gouretski & Koltermann, 2004). Daily-averaged output, obtained by first accumulating quantities at every model time step, was used in our analyses for the period 2005 to 2009; the output includes the total heat flux covariance terms (see Equation 3).

2.1.2. 0.08° Arctic Ocean HYCOM—CICE 4

The second model used in this study results from numerical experiments by Dukhovskoy et al. (2019) conducted using regional 0.08° Arctic Ocean (Bleck, 2002; Chassignet et al., 2003, 2007) coupled to CICE4. This simulation is referred to as HYCOM in the text.

The model domain is a subset of the 0.08° global HYCOM (Chassignet et al., 2009; Metzger et al., 2014) north of 38°N. The computational grid of the 0.08° HYCOM-CICE is a Mercator projection from the southern boundary to 47°N. North of 47°N, it employs an orthogonal curvilinear Arctic dipole grid (Murray, 1996). The model has effective spacing of ∼4–5 km in the Subpolar North Atlantic. The model topography is derived from the Naval Research Laboratory Digital Bathymetry Data Base 2-min resolution (NRL DBDB2). In the current configuration, HYCOM employs a vertical grid with 41 hybrid layers that provide higher resolution in the upper 1500 m. HYCOM's vertical hybrid grid is fixed neither in time nor in space; the vertical grid transitions from isopycnal or geopotential coordinates to terrain-following vertical grid over the shelves. In this configuration, 10 layers are distributed in the upper 38 m, and 20 layers in the upper 125 m. This simulation is one-way nested within the 0.08° Global HYCOM + Navy Coupled Ocean Data Assimilation (NCODA) 3.0 reanalysis (Metzger et al., 2014) (for 1993–2005) and Global Ocean Forecasting System (GOFS) 3.1 analysis (for 2006–2016).

Atmospheric forcing fields are obtained from the National Centers for Environmental Prediction (NCEP) Climate Forecast System Reanalysis (CFSR, horizontal resolution of 38 km) (Saha et al., 2010) for 1993–2011 and CFSv2 (Saha et al., 2014) for 2012–2016. This simulation was initialized from a spin-up simulation that, in turn, was initialized using climatological ocean temperature and salinity fields from the Generalized Digital Environmental Model version 4 (Carnes et al., 2010). More details on the model configuration and computational grid as well as model validation and analysis of the model experiments are given by Dukhovskoy et al. (2019, 2021). We use daily-averaged output from 2005 to 2009 for our analysis; unlike in POP, the total heat flux covariance term was not saved.

2.2. Volume and Heat Flux Definitions

The volume and heat fluxes used in this study are both calculated by integrating along a transect and over depth using daily means of velocity from the two models. When calculating the total flux through a strait or into a control volume, we consider the flux to be a transport. Transects extend along the continental shelf break in sections that are delineated by cross-shelf "gates". The net volume flux across the shelf break is defined as

$$V_{SB} = \int_H^0 \int_0^L \hat{v} \, d\hat{x} \, dz,$$ (1)

where $\hat{x}$ is the along-boundary direction and $\hat{v}$ is the velocity component perpendicular to the transect, H is the depth of the transect, and L is the length of the transect. In the case of the shelf break transect, the positive normal direction, n, is defined such that $\hat{v} = \mathbf{v} \cdot \mathbf{n} > 0$ is onto the shelf. In the case of the gates, the volume flux is calculated similarly, but the normal direction is northward. This allows us both to look at the overall volume flux onto the shelf and to construct budgets for the individual shelf regions by considering whether the gate is at the northern or southern boundary of the region. If the gate is the northern boundary, the normal direction must be reversed to point into the box.

The shelf break transect was defined separately for each model based on its bathymetry. The objective was to define a continuous contour that surrounded the Greenland continental shelf. Initially the 800 m isobath was used to define the shelf break, but the contour was adjusted to accommodate the connections to other continental shelves at the Davis and Denmark Straits where the shelf break is shallower than 800 m. The contour was also adjusted to include deep troughs, such as Kangerdlugssuaq Trough, which extend onto the continental shelf. The differences in the bathymetry and resolution of the models as well as specific choices about what deep or shallow regions to include results in differences in the shelf break transects.

Heat flux is calculated using daily means of potential temperature and velocity from both models. For the heat flux across the shelf break we define

$$\Phi_{SB} = \int_{H}^{0} \int_{0}^{L} \rho c_p (\theta - \theta_{ref}) \hat{v} \, d\hat{x} \, dz, \tag{2}$$

where ρ is the density of seawater, c_p is the specific heat capacity of seawater, θ is the potential temperature at the shelf break and θ_{ref} is the reference potential temperature. We have used a reference temperature $\theta_{ref} = -1.8°C$, which is the salinity-independent freezing temperature in POP (R. Smith & Gent, 2002). This definition is used both for the flux across the shelf break (Φ_{SB}), and through the various gates (Φ_G). As with the volume flux, positive heat flux is onto the shelf, and gate fluxes are positive in the northern and eastern directions. The choice of reference temperature does not change the net heat transport into an enclosed region (Bacon & Fofonoff, 1996; Schauer & Beszczynska-Möller, 2009).

We can decompose the heat flux into mean and eddy components through a Reynolds decomposition

$$\overline{v\theta} = \overline{v}\,\overline{\theta} + \overline{v'\theta'} \tag{3}$$

where $\overline{v}$ is the monthly average velocity and $v' = v - \overline{v}$. With this decomposition, we can quantify the contribution to shoreward heat flux from processes with timescales less than 1 month, such as mesoscale eddies or topographic Rossby waves. In POP, the covariance term ($v\theta$) is calculated at every model time step and saved as a monthly average. In HYCOM, this term is not saved, thus we must approximate this term from daily averages.

Figure 2 shows the 5-year average of the vertically-integrated volume (2a for POP and 2d for HYCOM) and heat (2b for POP and 2e for HYCOM) fluxes from each simulation for every 100 km section of the shelf break transect encircling Greenland. Along the transect, key locations are indicated to show which regions have the strongest fluxes and warmest temperatures. The average temperature at the shelf break in each section is shown in Figures 2c (POP) and 2f (HYCOM). In both simulations, the strongest on-shelf flux is near the Denmark Strait to its south, with weak on-shelf flux north of the strait and mostly off-shelf flux over the West Greenland shelf break. The magnitudes of the fluxes and their variability differ between the two simulations. From the Denmark Strait to the Davis Strait, HYCOM has warmer water (Figure 2f) at the shelf break, with less variability in temperature compared to POP (Figure 2c). Combined with stronger volume fluxes in HYCOM (Figures 2d vs. 2a) the result is greater magnitude heat fluxes in HYCOM (Figures 2e vs. 2b). While the HYCOM simulation does not have the same temporal variability as POP, there is along-transect variability where regions of strong off-shelf flux are adjacent to those with strong on-shelf flux. In POP, the temporal variability (shown here by the 20th to 80th percentile range) is large relative to the mean between Sermilik Gate and the Denmark Strait. Eddies traveling along the shelf break in this region could explain some of this variability, as discussed further in Section 3.2.

The models do not agree on the sign of volume or heat flux across the shelf in each 100 km section. This is likely the result of differences in the modeled circulation, and the sensitivity of these results to the particular part of the continental shelf break sampled.
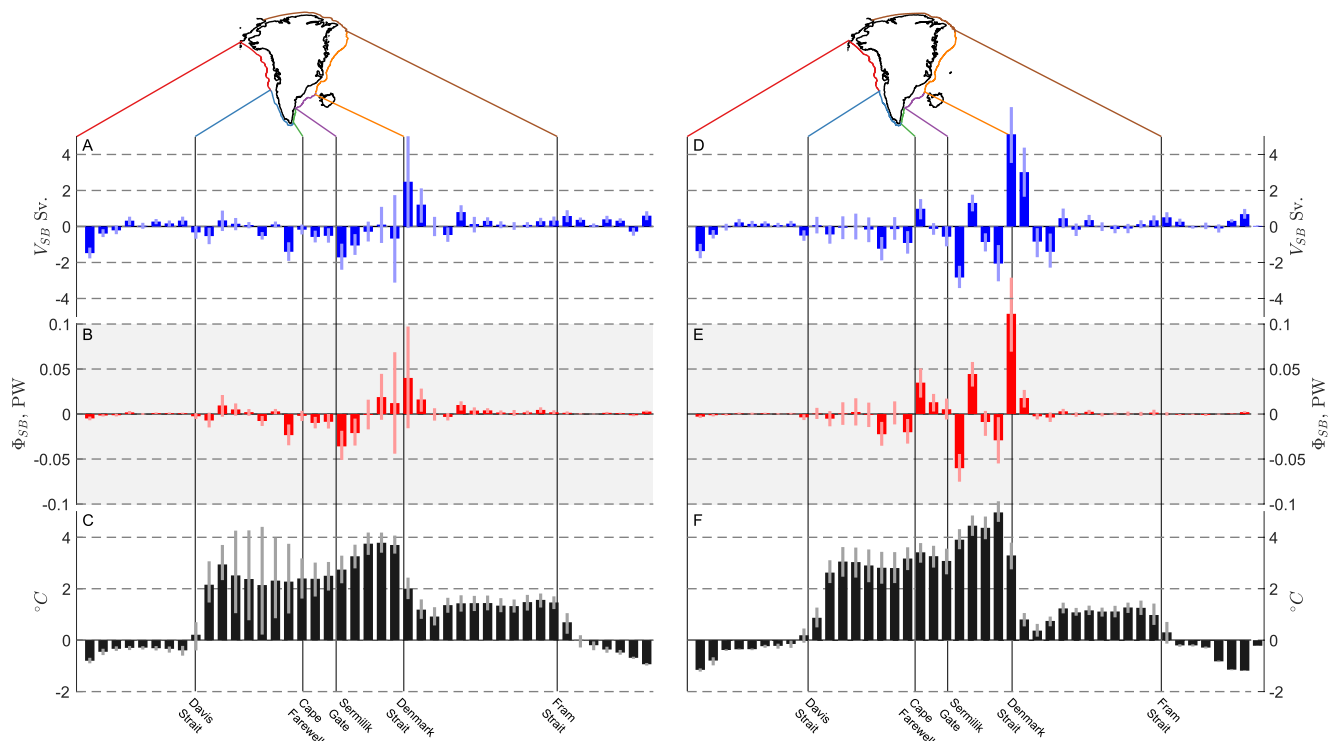
Figure 2. Bar graphs of net volume fluxes (Sv, blue), net heat fluxes (PW, red), and average temperature (°C, black) for every 100 km section of the transect encircling Greenland for POP (A–C) and HYCOM (D–F). For both volume and heat fluxes, positive values indicate flux onto the continental shelf. Dark bars are the 5-year averages from 2005 to 2009, with light bars representing the 20th and 80th percentile range. In both models, the strongest on-shelf fluxes are near the Denmark Strait. In POP this maximum is associated with strong variability; in HYCOM the heat flux is consistently onto the shelf at this location.

2.3. Continental Shelf Control Volumes

To understand how warm salty Atlantic water crosses onto the shelf and where it is present, the shelf and shelf break must be clearly defined. Shallow straits and deep troughs make choosing a single isobath to represent the shelf break challenging. Based on Figure 2, we limit our focus to the southern shelf break, extending from Davis Strait to Denmark Strait (see Figures 3a and 3b), where the strongest on- and off-shelf heat and volume fluxes occur. The exact depths of the shelf break transect in each model (see Figures 3c and 3d) show how the bathymetry of the two simulations differs. See Figure S1 in Supporting Information S1 for a detailed map of the Southeast region highlighting the troughs and small scale bathymetry.

In addition to the shelf break, we define three control volumes to examine spatial differences in cross-isobath fluxes and properties on the shelf. The contour begins at the Davis Strait (0 km), and the along-transect distance used in this paper is measured from that point counterclockwise, first south along western Greenland then north along eastern Greenland. We subdivide the shelf break into three regions: from Davis Strait to Cape Farewell, Cape Farewell to the Sermilik Gate, and the Sermilik Gate to the Denmark Strait. The gates are labeled in Figures 3a and 3b, and span the shelf from the coast to the shelf-break contour. Between these gates we define the regional control volumes of the continental shelf as: (a) Southwest, (b) Narrow Shelf, and (c) Wide Shelf. The Southeast region has been subdivided into the Narrow and Wide sections because of differences in the cross-shelf exchange that we calculated along the shelf break. The Cape Farewell Gate is located at the same position as the Overturning in the Subpolar North Atlantic Program (OSNAP) mooring array at 60°N (Le Bras et al., 2018).

2.4. Model Intercomparison: Velocity and Temperature

Before focusing on the heat fluxes across the shelf, we compare the velocity and temperature around the Greenland continental shelf in the two simulations. The goal of the comparisons is to provide context for the differences in cross-shelf fluxes between the two simulations. We also refer to observations to provide further context or show possible model biases but the goal of this section is not to validate either simulation. To calculate the differences, both the POP and HYCOM outputs are interpolated onto a uniform 1/10° degree grid.
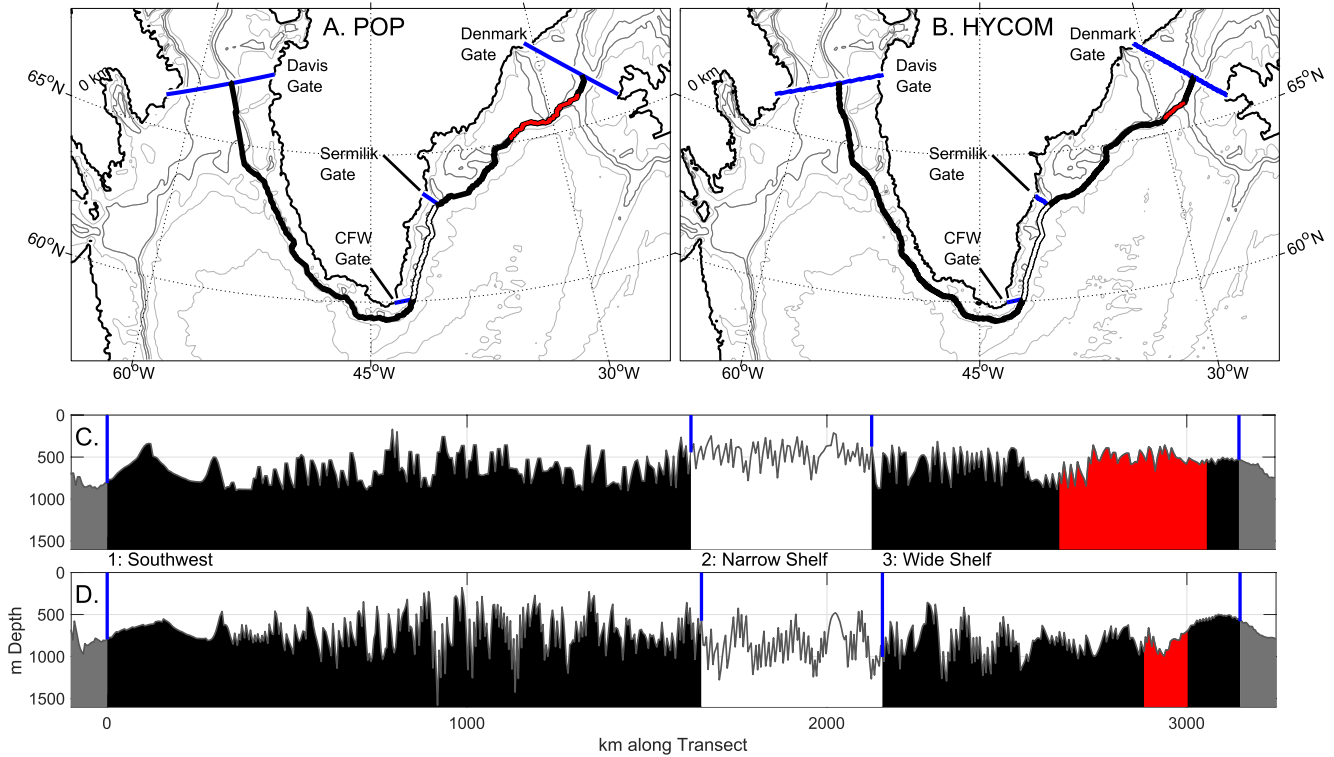
Figure 3. Map of shelf break transects in (a) POP and (b) HYCOM, subdivided at the major straits and gates and plotted over the regions' bathymetries. The exact depth along the transect plotted for (c) POP and (d) HYCOM with the regions numbered. Shelf regions are: (1) Southwest, (2) Narrow Shelf, and (3) Wide Shelf. The color of the transect in each region corresponds to the bathymetry plotted for that region. The red line highlights the region of the shelf where we observe the propagating high-frequency signal discussed in Section 3.2. A regional map of the Southeast region directly comparing the two bathymetries is provided in Figure S1 in Supporting Information S1.

The mean surface circulation for 2005–2009 is shown for both models in Figures 4a and 4b; depth-averaged velocity over the upper 15 m of the water column is considered to be the surface flow. Both models show the observed structure of the East Greenland/Irminger Current merging at Cape Farewell (Le Bras et al., 2018). On the shelf, the complex structure of the East Greenland Coastal Current is better represented in POP (Bacon et al., 2014; Sutherland & Pickart, 2008). At 60°N, at the Cape Farewell Gate, the black line in Figures 4a and 4b, the peak velocity in HYCOM is 64 cm s^{-1} at a position 120 km from the coast. In POP there are two peaks in the surface speed: 35 cm s^{-1} located 97 km from the coast and 42 cm s^{-1} located 155 km from the coast. The average velocity along the shelf at the Cape Farewell Gate is included in Supporting Information S1 (Figure S2). This difference in current structure contributes to the difference in net transport onto the shelf between the two models (Figures 6a–6b). In POP, the coastal currents are stronger and the shelf slope currents are weaker in the southeast region (Figure 4c). However, the West Greenland Current has a stronger core that is shifted farther off the shelf in POP compared to HYCOM.

We calculate the EKE from the daily averages of model velocity. We define EKE as:

$$\text{EKE} = \frac{u'^2 + v'^2}{2} \tag{4}$$

with $u' = u - \overline{u}$, where u is the daily average velocity and $\overline{u}$ is the monthly average of velocity. This formulation defines eddies as anomalies that have a period between 2 days and 1 month. We use only the depth-averaged velocity in the top 15 m. The 2005–2009 average is plotted in Figures 4d and 4e. In both models, west of Greenland there is an expanse of elevated EKE extending into the central Labrador Sea (outlined in black in Figures 4d and 4e). Elevated EKE values in the Labrador Sea in POP are limited to deep water offshore of the Southwest Shelf; in contrast, HYCOM has elevated EKE both on the Southwest Shelf as well as off the shelf, possibly indicating a difference in the cross-shelf exchange between the two models in this region. EKE estimated from TOPEX/Poseidon satellite altimetry (Brandt et al., 2004) and surface drifters (Fratantoni, 2001) in this region
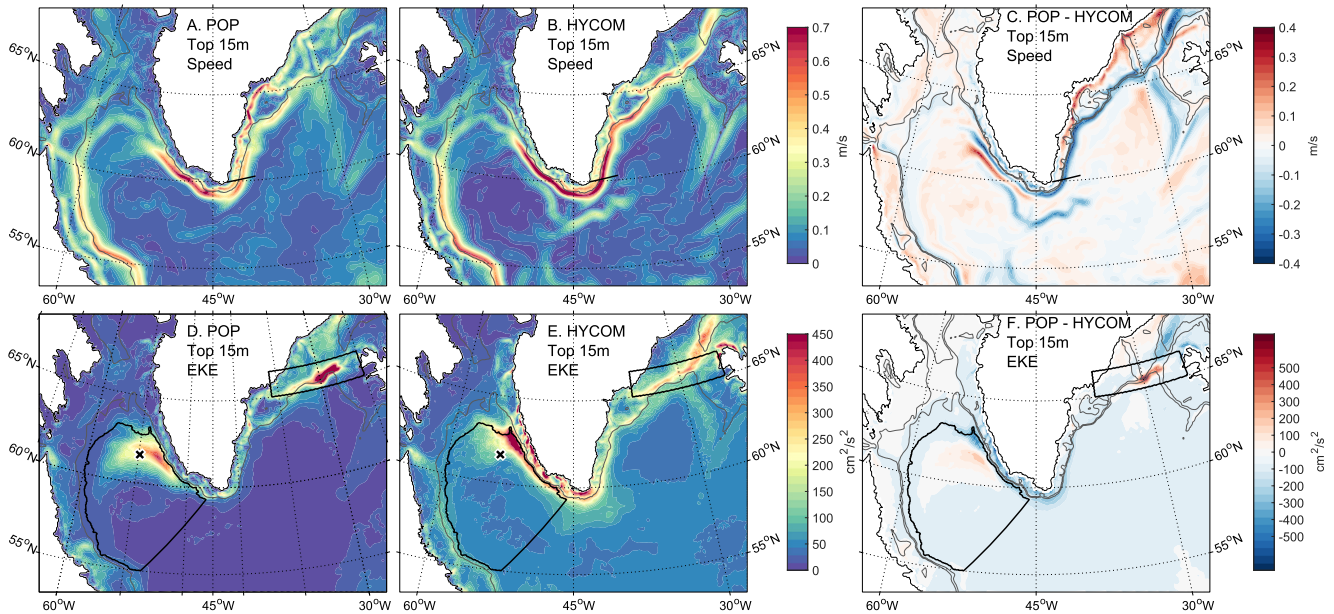
Figure 4. Average speed in the top 15 m over 2005–2009 for POP (a), HYCOM (b), and POP-HYCOM (c). Average Eddy Kinetic Energy over the same period in the top 15 m over 2005–2009 for POP (d), HYCOM (e), and POP-HYCOM (f). In (a,B,C) the black line shows the transect at 60°N. In (d, e, f) the boundary of two control volumes are shown in black: the interior Labrador Sea defined by the 2,000 m isobath and a box at the Denmark Strait. The black x in (d), (e) is the location of the maximum EKE in the drifter derived data set.

shows a similar pattern of elevated EKE in the eastern Labrador Sea; though neither observation-derived estimate is directly comparable to the EKE calculated from the simulations. The surface EKE from Brandt et al. (2004) in the West Greenland Current ranges from 400 to 800 cm² s⁻² for the period 1997–2001. Altimeter-based estimates are generally higher than those in either simulation, but are calculated from sea-surface height gradients and the resulting geostrophic velocities, while the model EKE includes both geostrophic and ageostrophic velocities.

An EKE climatology (1979–2015) from 15 m drogued and undrogued satellite-tracked surface drifters available from the Atlantic Meteorological and Oceanic Laboratory of the National Oceanic and Atmospheric Administration (Laurindo et al., 2017) can be used to provide a qualitative comparison with the simulated fields. Figure 5 shows the speed and EKE from observations for the same region as Figure 4. Areas with fewer than 90 drifter days per unit area are not plotted in Figure 5; the continental shelves are the primary region excluded. In the

Figure 5. EKE climatology (1979–2015) from 15 m drogued and undrogued satellite-tracked surface drifters (Laurindo et al., 2017). The black x indicates the location of maximum EKE in the interior Labrador Sea and the boundary of two control volumes are shown in black: the interior Labrador Sea defined by the 2,000 m isobath and a box at the Denmark Strait.

eastern Labrador Sea, the EKE is 400–500 cm² s⁻², which is consistent with the maximum EKE of both models. The maximum EKE within the defined interior Labrador Sea control volume in the AOML data set is 570 cm² s⁻² and the location is marked with an "x" in Figures 5 and 4d–4e. In the Labrador Sea, the maximum EKE in POP is 437 cm² s⁻², while in HYCOM it is 624 cm² s⁻². The 2005–2009 average EKE in the central Labrador Sea (outlined in black in Figure 4e) in HYCOM is 80.8 cm² s⁻², with the 20th to 80th percentiles ranging from 46.7 to 82.3 cm² s⁻². The POP values indicate lower EKE with a larger range: mean EKE is 56.8 cm² s⁻², with 20th to 80th percentiles from 13.2 to 92.0 cm² s⁻². The EKE fields depicted by the two simulations have similar magnitudes and patterns as those observed in the Labrador Sea, but the region of elevated EKE in HYCOM is farther north (4E and F) than in POP or in the AOML drifter-derived EKE.
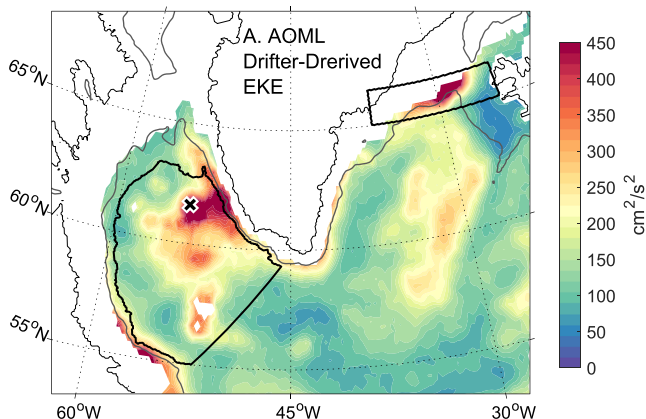
There is a second region of elevated EKE where the Irminger Current retroflects south of the Denmark Strait. This EKE patch corresponds to a region of large sea surface height anomalies observed by AVISO (Trodahl & Isachsen, 2018) and is also present in the drifter-derived EKE estimate (Figure 5). Heightened EKE near the Denmark Strait is also consistent with observations of mesoscale eddies and boluses formed at the Denmark Strait
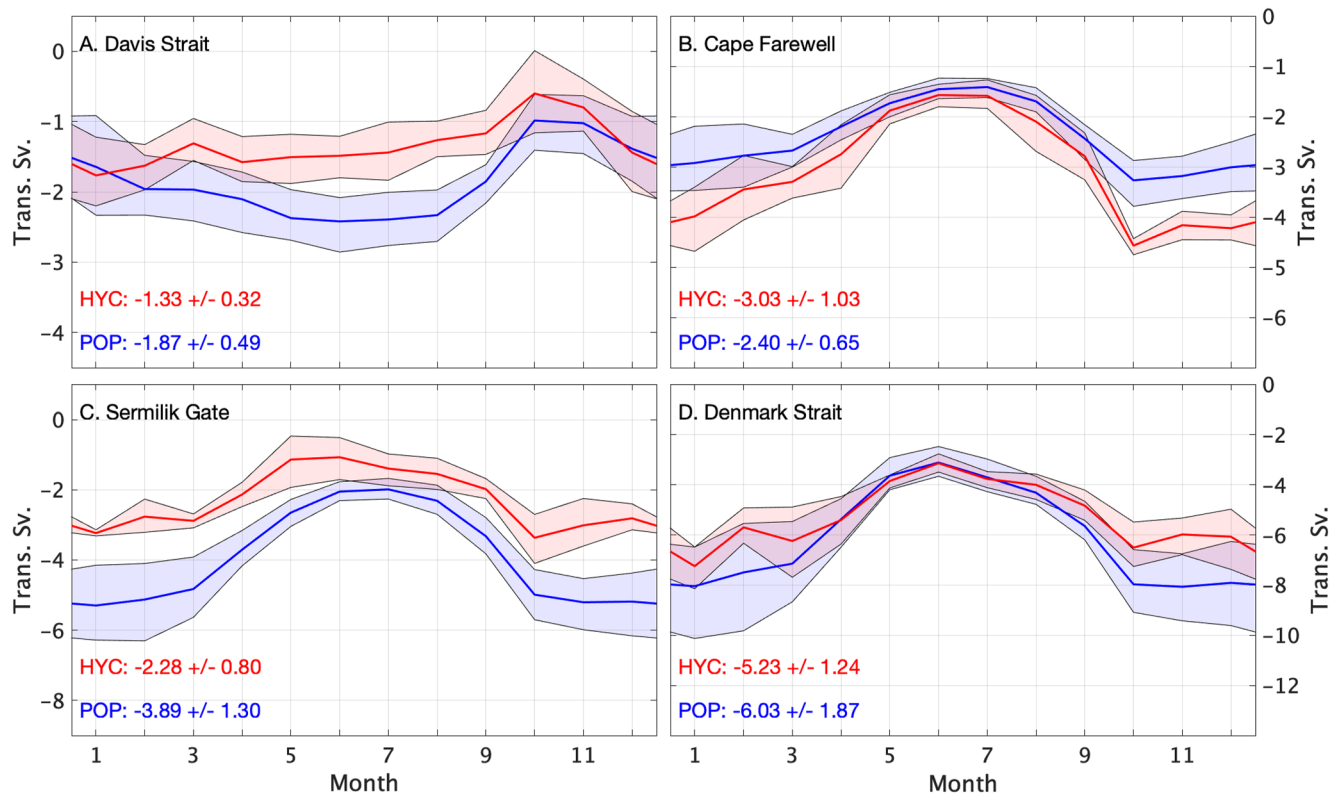
Figure 6. Volume transports through straits defined in Figure 3 from POP (blue) and HYCOM (red) and with the shaded region showing the 20th-80th percentile range; the annual mean and standard deviation are included on each plot. Transports are from (a) Davis Strait (b) Cape Farewell Gate (c) Sermilik Gate (d) Denmark Strait; here strait refers to the entire transect between two land masses and gate refers to the area between the Greenland coast and the defined shelf break. Negative transport is southward.

overflow (Moritz et al., 2019). The 2005–2009 average EKE in the defined box just south of the Denmark Strait (outlined in black in Figures 4c and 4d) is similar in POP (139 cm^2 s^{-2}) and HYCOM (131.7 cm^2 s^{-2}), but the maximum EKE in POP (968 cm^2 s^{-2}) is twice the maximum in HYCOM (397 cm^2 s^{-2}). In the POP field, there is a particularly strong band of EKE just south of the strait at the shelf break, while in the HYCOM field the maximum is broader and is located to the north of the strait.

Volume transport through key straits in the two models can be used to further understand circulation differences in the simulated oceans. The 2005–2009 average of transport for each month is plotted in Figure 6 for: Davis Strait (Figure 6a, from Canada to Greenland), Cape Farewell Gate (Figure 6b, Greenland to the shelf break contour), Sermilik Gate (Figure 6c, Greenland to the shelf break contour), and Denmark Strait (Figure 6d, Greenland to Iceland). Here, "strait" refers to the entire transect between two land masses, and "gate" refers to the area between the Greenland coast and the defined shelf break. At the Davis Strait, the average volume transport for 2005–2009 in HYCOM is $V_{DS} = -1.33 \pm 0.23$ (1 Sv = 10^6 m^{3}s^{-1}), and in POP $V_{DS} = -1.87 \pm 0.49$. Curry et al. (2014) found the Davis Strait volume transport to be -1.6 ± 0.5 Sv from observations for 2004–2010. On the shelf, the 5-year average volume flux at Cape Farewell is $V_{G:CFW} = -3.03 \pm 1.03$ in HYCOM and $V_{G:CFW} = -2.40 \pm 0.65$ in POP. At the Cape Farewell Gate the winter maximum volume transport in HYCOM is 1 Sv greater than the maximum in POP. Observations from the OSNAP east array, the same location as the Cape Farewell Gate, showed the average transport of the EGC from 2014 to 2016 to be -3.5 ± 0.5 Sv (Le Bras et al., 2018). The 5-year average transport at the Sermilik Gate in HYCOM is $V_{G:SG} = -2.28 \pm 0.80$, while in POP it is $V_{G:SG} = -3.89 \pm 1.03$. The winter maximum at Sermilik gate is weaker in HYCOM compared to POP by roughly 2 Sv, but the difference in the summer minimum is less than 1 Sv. From observations of the of the East Greenland Coastal Current collected at a similar location as the Sermilik Gate, Bacon et al. (2014) report a February maximum transport of 3.8 Sv and an August minimum transport of 1.9 Sv. The 5-year average net transport through the Denmark Strait is $V_{Dmk} = -5.23 \pm 1.24$ in HYCOM and $V_{Dmk} = -6.03 \pm 1.87$ in POP. The summer transport through the Denmark
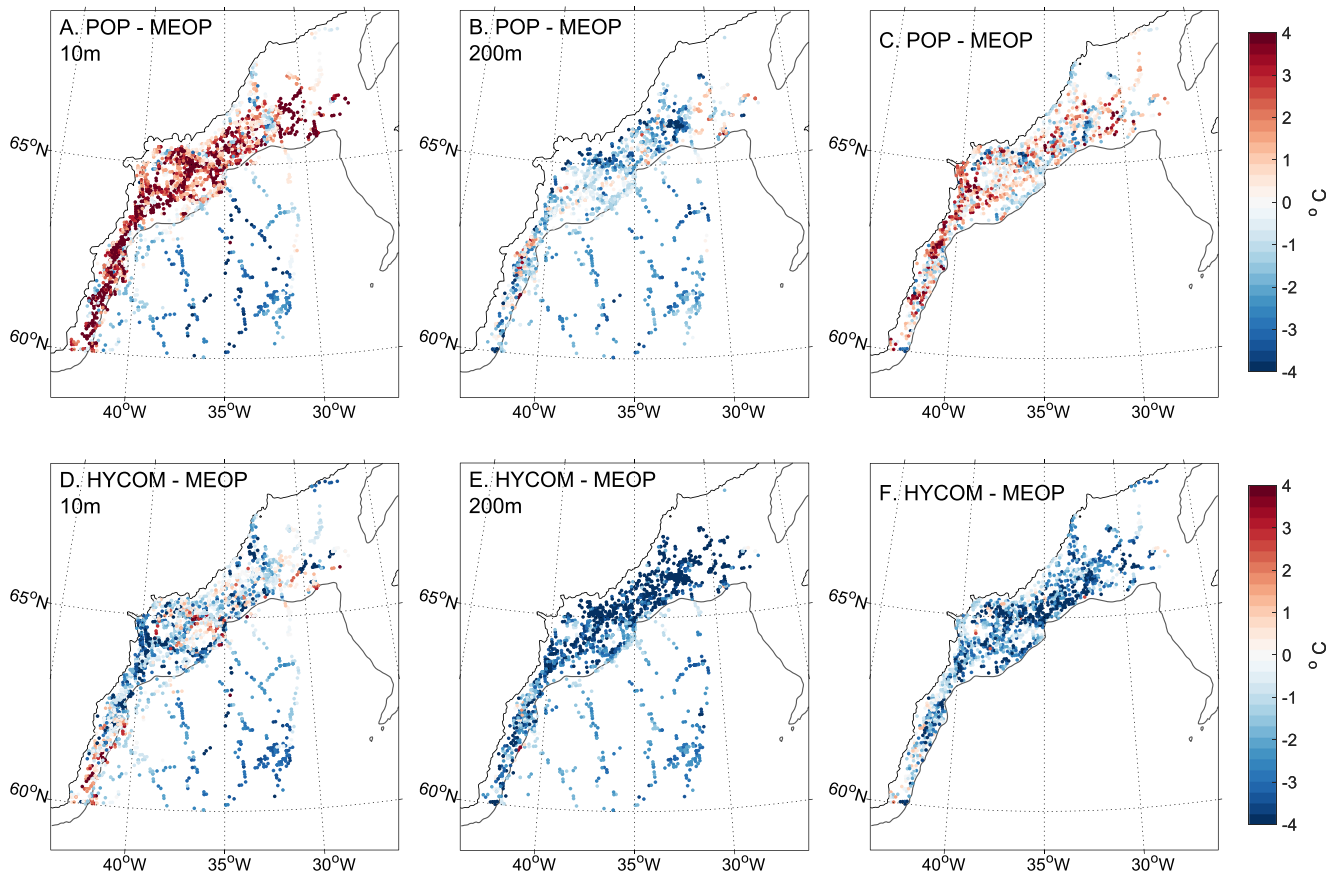
Figure 7. Comparisons of temperature from MEOP profiles and either the HYCOM or POP simulations over the southeast Greenland shelf and the Irminger Sea: (a) difference (POP-MEOP) in surface temperature (10 m), (b) difference (POP-MEOP) in temperature at 200 m, and (c) vertically-averaged difference (POP-MEOP) in temperature over the continental shelf, (d) difference (HYCOM-MEOP) in surface temperature (10 m), (e) difference (HYCOM-MEOP) in temperature at 200 m, and (f) vertically-averaged difference (HYCOM-MEOP) in temperature over the continental shelf.

Strait is very similar between the two simulations, but the winter maximum transport can be 1–2 Sv greater in POP. The net transport through the Denmark Strait as estimated by Østerhus et al. (2019) is 4.3 Sv southward.

We compare the simulated continental shelf temperatures to potential temperature measurements from animal-borne instruments from the Marine Mammals Exploring the Oceans Pole to Pole (MEOP) project (Treasure et al., 2017). The data used for comparison are vertical profiles of temperature collected during the upward transit of the instrumented animal. Of the used profiles, 75% of the data were from 0 to 200 m and 90% were from 0 to 420 m. The deepest profile was 1,332 m. We compare them to model temperature profiles between 60°N and 70°N and 45°W to 27°W. Between 2005 and 2008, a total of 3,382 observational profiles were recorded in our defined volume. For each MEOP profile, we extract a vertical profile from the concurrent monthly average temperature field from each simulation at the closest model grid point to where the MEOP profile was taken. MEOP data was interpolated onto the model grids to calculate differences in the simulated and observed temperatures.

At the surface (10 m), POP is warmer than MEOP on the shelf and cooler in the Irminger Sea (Figure 7a). However, at 200 m, POP is generally cooler everywhere (Figure 7b). The vertically-averaged difference in temperature shows the warm bias at the surface is greater than the cold bias at depth (Figure 7c). Over the Wide Shelf, POP is 0.31°C warmer than MEOP; over the Narrow Shelf, the warm bias is 0.86°C. HYCOM is colder than the MEOP profiles over all (Figures 7d–7f), but shows some warm biases in the surface layer (Figure 7a). The bias over the Wide Shelf is −2.5°C, and over the Narrow Shelf the bias is −1.5°C. In POP, the temperature bias is used to calculate a bias in heat content of 1.3 and 3.5 MJ in the Wide and Narrow Shelf regions, respectively. In HYCOM, the difference in temperature results in an on-shelf heat content that is −6.0 and −10.1 MJ lower than expected from observations in the Wide and Narrow Shelf regions, respectively.

Table 1
Average (2005–2009) Fluxes Through Gates and Across the Shelf

Section	Length (km) POP	Length (km) HYCOM	V (Sv) POP	V (Sv) HYCOM	Φ (TW) POP	Φ (TW) HYCOM	T_{avg} (°C) POP	T_{avg} (°C) HYCOM
Davis Gate	166	192	0.25 ± 0.74	-0.27 ± 0.59	8.52 ± 13.2	-7.85 ± 9.73	–	–
Southwest Shelf	1,622	1,651	-2.40 ± 0.79	-2.15 ± 0.84	-29.9 ± 10.4	-16.6 ± 16.0	1.96 ± 1.36	1.96 ± 0.84
			$(-23.8, 21.4)$		$(-420, 390)$			
Cape Farewell Gate	77	62	-2.62 ± 0.75	-2.45 ± 0.85	-38.7 ± 19.8	-33.4 ± 18.6	–	–
Narrow Shelf	503	503	-1.13 ± 0.62	-0.59 ± 0.45	-18.0 ± 13.9	28.2 ± 15.7	1.65 ± 1.02	1.41 ± 0.81
			$(-15.4, 14.3)$		$(-329, 311)$			
Sermilik Gate	74	87	-3.53 ± 1.20	-3.03 ± 1.12	-53.2 ± 21.6	-39.5 ± 21.9	–	–
Wide Shelf	1,021	994	-0.90 ± 0.66	0.77 ± 0.76	16.4 ± 13.8	55.0 ± 23.3	2.15 ± 0.64	0.95 ± 0.55
			$(-40.6, 39.7)$		$(-930, 946)$		.	
Denmark Gate	257	361	-4.07 ± 1.42	-2.28 ± 0.95	-33.2 ± 18.9	-13.0 ± 8.43	–	–

Note. Summary of key volume and heat fluxes and control volume temperatures. Cross-shelf heat and volume fluxes (Southwest Shelf, Narrow Shelf, and Wide Shelf) are positive onto the shelf. Gate heat and volume fluxes (Davis Gate, Cape Farewell Gate, Sermilik Gate, and Denmark Gate) are positive northward; note that for gates we consider only flux between the coast and the continental shelf break. Columns 1 and 2 are the length of each section in POP and HYCOM. Columns 3–6 are the 2005–2009 average volume and heat fluxes with an uncertainty of one standard deviation for POP and HYCOM. Columns 7 and 8 are the 2005–2009 volume average temperature of each on shelf control volume. For POP, the average net on and off shelf volume and heat fluxes for each portion of the shelf break in parentheses below the average net fluxes.

The seasonal cycle of the 2005–2009 average of heat content of the on-shelf control volumes was also calculated for both models. In the Southwest Region, the average heat content on the shelf is similar between the two simulations for most of the year, except from August-November when the heat content on the shelf is greater in POP. The heat content maxima in both models agree with observations, which have shown the warmest water being present on the shelf between September and January (Grist et al., 2014). Over the Narrow Shelf, the average heat content in POP is 2.47 MJ greater than the average in HYCOM. On the Wide Shelf, the heat content in the two simulations differs by 5.64 MJ on average, but has a similar seasonal range and standard deviation. The maximum heat content in the Wide Shelf region occurs in September in both simulations; this is in general agreement with Gillard et al. (2020) who found the summer months (July-August) to be the warmest time of year in the Helheim Troughs (near the Sermilik Troughs) and the fall months (September-November) to be the warmest time of year in Kangerdlugssuaq trough. For both the Narrow and Wide shelf, the difference in the annual average heat content between POP and HYCOM is less than what was found based on the MEOP profiles alone. This is likely because the MEOP data have a seasonal bias; 49% of the profiles used in these comparisons were collected in June, July, or August. During these months, the difference in heat content on the Narrow Shelf in POP and HYCOM is comparable to the difference expected from the comparison to the MEOP data. Direct calculation of the heat content on the shelf is consistent with the conclusion that the Southeast shelf is too warm in POP and too cold in HYCOM.

In summary, generally the mean currents are stronger along the shelf break in HYCOM compared to POP. The EKE results indicate that POP is more energetic than HYCOM, particularly near the Denmark Strait. EKE estimated from surface drifters shows a pattern of elevated EKE in the WGC eddy shedding region that is similar to both models with some difference in the location of maximum eddy activity. The volume transport through the straits and gates do not show one simulation to be closer to observational estimates than the other. The bias in temperature is smaller in POP compared to HYCOM, and where the shelf waters are too warm in POP, they are too cold in HYCOM. As well, there is a stronger cross-shelf temperature gradient in HYCOM than in POP.

3. Cross-Shelf Heat Transport Along the Southern Greenland Coast

3.1. Mean Cross-Shelf Fluxes

Net volume and heat fluxes through each section and gate around Southern Greenland are listed in Table 1. In POP the only region of net heat flux onto the shelf is along the Wide Shelf. In HYCOM there is net heat flux onto

the shelf over both the Wide and Narrow Shelf regions. This is consistent with Figures 2b and 2e. In both POP and HYCOM, there is less heat flux at Cape Farewell than at the Sermilik Gate indicating that the Narrow Shelf is a region of heat loss, despite it being a region of net on-shelf heat flux in HYCOM.

Along the west Greenland slope, we expect to see off-shelf volume and heat flux in agreement with previous studies (e.g., Böning et al., 2016; Dukhovskoy et al., 2019; Myers et al., 2009; Schulze Chretien & Frajka-Williams, 2018). Cross-isobath heat flux is negative in the Southwest region, consistent with the source of heat to this region originating from southward heat flux at Cape Farewell or surface heat fluxes. Both simulations are consistent in this region, with weak seasonal cycles of heat and volume flux. The volume-averaged shelf temperature of the Southwest region is highly variable, and the fall peak is the warmest volume-average temperature of any region. The presence of warm ocean water in this region is consistent with observations of ocean-driven melting of the ice sheet in west Greenland. (See Straneo & Cenedese, 2015; for an review.) Correlation between the heat flux at the Cape Farewell Gate and heat content in the Southwest region is 0.87 in POP and 0.74 in HYCOM; both are significant at a 0.05 significance level. Using the surface heat flux time series saved from the POP simulation, we find that the net surface heat flux and heat content in the Southwest region are out of phase, resulting in a low correlation. In both models, heat flux through the Cape Farewell Gate (Figure 6b) as well as the shelf temperature peak in the fall; in POP, the net surface heat flux is highest in the summer.

3.2. Eddy Cross-Shelf Fluxes

Heat fluxes across the shelf along the southern transect display variability on time scales of several days. Figures 8a and 9a show five-month-long Hovmöller diagrams of temperature at 200 m in 2005 for each model at the shelf break, illustrating the seasonal progression of warm water from the Denmark Strait to Davis Strait. To reduce noise in all variables from currents meandering across the isobath, a 50 km boxcar filter is applied. Hovmöller diagrams of 200 m temperature for the full 5-year period are included in Figures S3 and S4 in Supporting Information S1.

At the Denmark Strait there is a front between the cold water to the north and the warm Atlantic water in the Irminger Current in both models (Figures 8a and 9a), but the water north of the front is much colder in HYCOM (Figure 9a) consistent with the average shelf temperatures in both simulations (-0.62 ± 0.17°C compared to 0.11 ± 0.37°C in POP for the section of the shelf between the Denmark and Fram Straits). The warmest water at the shelf break in both models is along the Wide Shelf region (between the Denmark and Sermilik Gates). In POP between Sermilik Gate and Cape Farewell seasonal warming occurs in May (Figure 8a). However, in HYCOM (Figure 9a), the temperature over this portion of the shelf break shows more high-frequency variability than seasonal change. These differences are consistent with the annual cycles of temperature in the Southwest region and heat flux through the Cape Farewell and Davis Gates. The seasonal timing of warming along the western shelf break is consistent with the results of Grist et al. (2014), who showed the warmest waters in that region from September to January.

In both models, there is a high-frequency signal generated at or intersecting the shelf break south of the Denmark Strait in roughly the same location as the cold-warm front (Figures 8a and 9a). In POP (Figure 8a), the origin of these signals is consistently 102 km south of the Denmark Strait. In HYCOM (Figure 9a), the position of the cold-warm front meanders and changes in strength over the months shown. These high-frequency signals are generated regularly throughout the year, see Figures S3 and S4 in Supporting Information S1 for the Hovmöller diagrams over the entire 5 years record. As these signals propagate along the transect they result in extreme on- and off-shore heat fluxes.

Figures 8b and 9b show the band-pass filtered vertically integrated heat flux, and Figures 8c and 9c show the spectra of the vertically integrated heat flux. In Figures 8b and 9b, lines are plotted with phase speeds of $c_p = 0.47$ m/s for POP and $c_p = 0.47$ m/s for HYCOM. In both models the heat flux spectra have peaks at high frequencies south of the Denmark Strait. In POP (Figure 8c), there are three localized regions of high-frequency variability, two with a frequency of about 0.30 days^{-1}, and one around 0.50 days^{-1}, the Nyquist frequency. In HYCOM (Figure 9c) the high-frequency peak is more localized ranging from 0.24 days^{-1} to 0.50 days^{-1}. Therefore, to isolate the heat flux associated with these propagating signals, the models were band-pass filtered with different ranges: for POP the range is 3–7 days, and for HYCOM it is 2–5 days. The band-pass filtered heat flux in both models (Figures 8b and 9b) shows a propagating signal, though the signal travels only 116 km in HYCOM, while
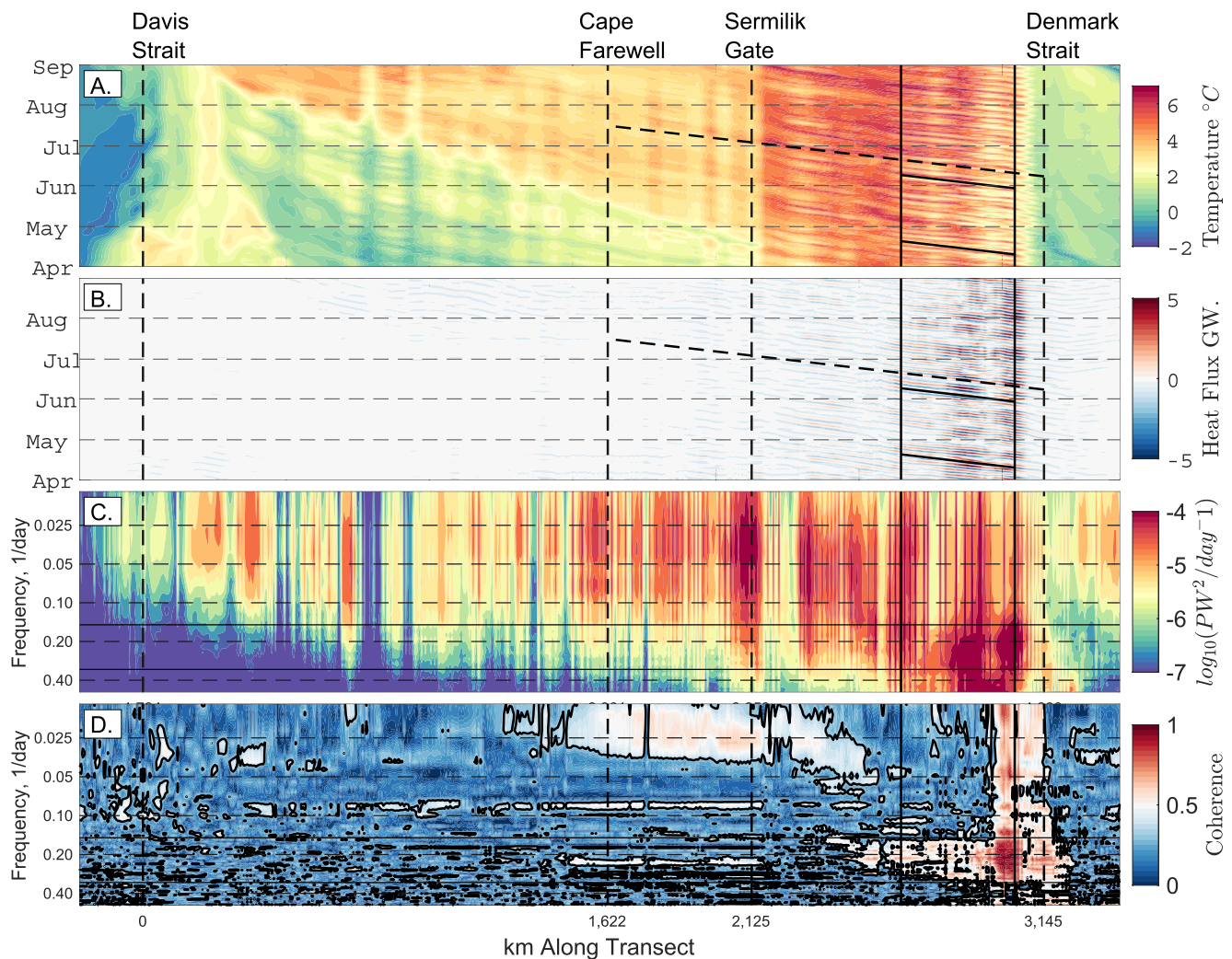
Figure 8. POP results showing:(a) Hovmöller diagrams from April–September 2005 of temperature at 200 m, (b) vertically integrated heat flux with a 3–7 days band pass filter, (c) spectra of heat flux at each location along the contour with horizontal lines showing the frequency band that was used to produce (b), and (d) coherence between heat flux at every location and 102 km south of the Denmark Strait. Vertical dashed lines show the locations of the gates, and solid vertical lines show the region of the propagating signal from 102 to 499 km south of the Denmark Strait, highlighted in red in Figure 3. The black contour in (d) is the threshold for coherence at the 0.10 significance level $\gamma_{XY}^2 = 0.35$. Error for the spectra are estimated using a χ^2 distribution with a 0.05 significance level such that the range between high and low error estimates is $\log_{10}(0.6)$.

in POP it continues for 397 km. Figure 3 shows the portion of the shelf where the propagating signal is strongest (shown in red in each model's map). The location where the signal dissipates in HYCOM (Figure 9b) coincides with the mouth of Kangerdlugssuaq Trough. In POP (Figure 8b) the signal dissipates on the northern end of the Sermilik Troughs. In both cases the dissipation or on/off-shelf shifting of the signal occurs where there is a change in bathymetry. In both models (Figures 8c and 9c), the high-frequency energy in the spectra of vertically integrated heat flux decays southward along the shelf.

The band-pass filtered vertically integrated heat flux is not the optimal way to identify mesoscale eddies. In Figures 8a and 9a, the propagating signal is apparent in the 200 m temperature much farther from the Denmark Strait than in the filtered heat flux. In the spectra, Figures 8c and 9c, there is energy in this high-frequency band along nearly the entire southeast shelf break. The magnitude of the impact on the vertically integrated heat flux is strongest from 102 to 499 km south of the Denmark Strait in POP and 154 to 271 km south of the Denmark Strait in HYCOM.

The coherence of the heat flux time series at each location along the transect and the heat flux at the location where the signal originates is shown in Figures 8d and 9d. The 0.10 confidence level for the coherence
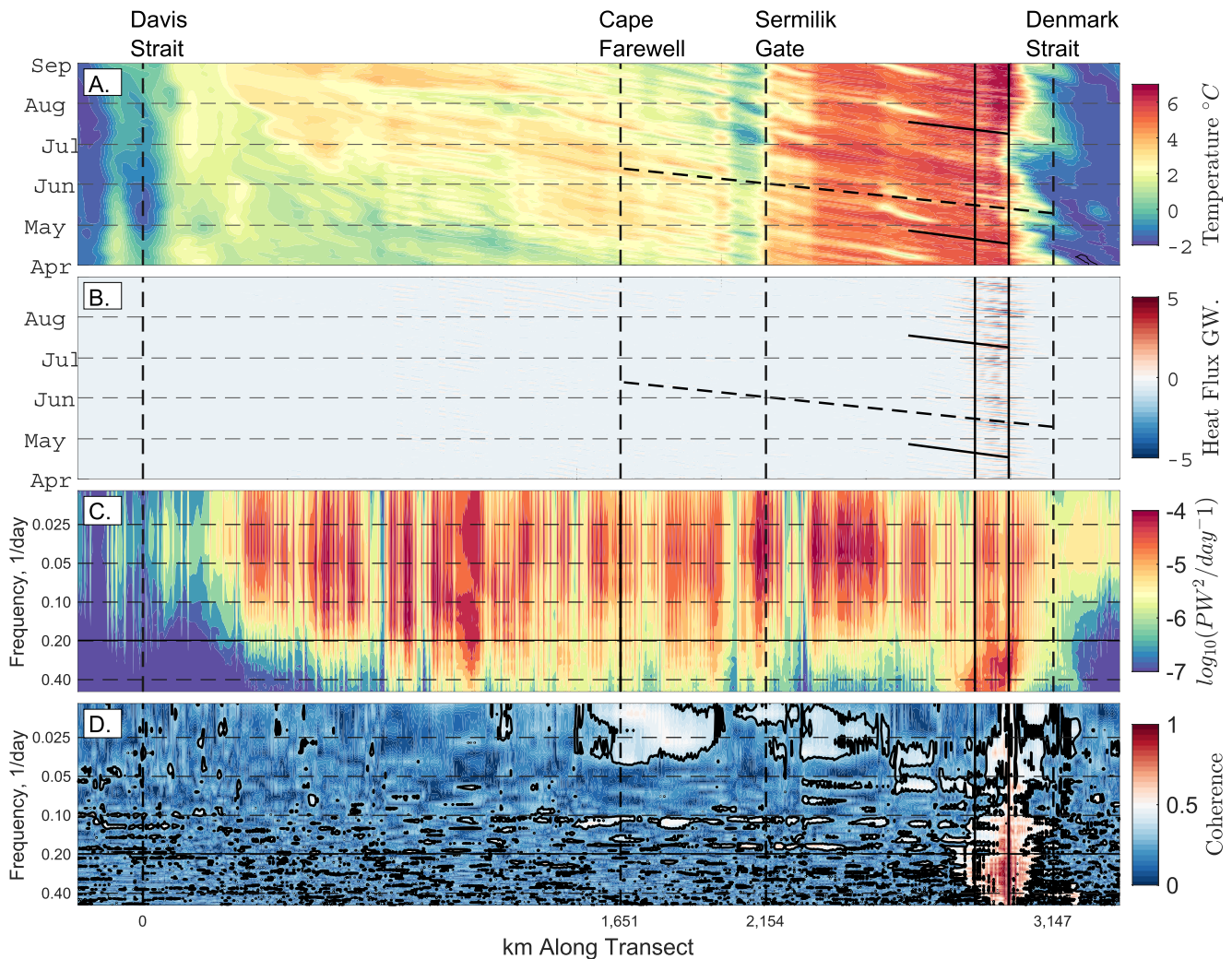
Figure 9. As in Figure 8. HYCOM results showing:(a) Hovmöller diagrams from April–September 2005 of temperature at 200 m, (b) vertically integrated heat flux with a 2–5 days band pass filter, (c) spectra of heat flux at each location along the contour with horizontal lines showing the frequency band that was used to produce (b), (d) coherence between heat flux at every location and 154 km south of the Denmark Strait, and (e) the associated phase. Vertical dashed lines show the locations of the gates, and solid vertical lines show the region of the propagating signal from 154 to 271 km south of the Denmark Strait, highlighted in red in Figure 3. The black contour in (d) is the threshold for coherence at the 0.10 significance level $\gamma_{XY}^2 = 0.35$. Error for the spectra are estimated using a χ^2 distribution with a 0.05 significance level such that the range between high and low error estimates is $\log_{10}(0.6)$.

squared is $\gamma_{XY}^2 = 0.35$, the black contour in both plots. These results are sensitive to the choice of the location where the signal originates due to the high grid-point to grid-point variability in the flux. For both models, there are regions of strong coherence both north (upstream, closer to the Denmark Strait) and south (downstream, farther from the Denmark Strait). The upstream coherence shows the possible origin of the signal. In HYCOM (Figure 9d), the coherence is not significant north of the Denmark Strait in the same narrow high-frequency band (0.24–0.5 days^{-1}). In POP (Figure 8d), the coherence is significant north of the Denmark Strait across most frequencies in the 3–7 days band. In both models, where the coherence is significant south of the Denmark Strait, the phase (not plotted) shows evidence of a propagating signal. In both POP and HYCOM, there is also significant coherence at a lower frequency ($f = 0.1$ day^{-1}) extending along the shelf to Cape Farewell beyond the defined regions of propagation. This could be associated with a shift in the speed of the eddies as they travel along the shelf. Both POP and HYCOM show a coherent signal at $f > 0.025$ days^{-1} along the Narrow Shelf region indicating that a lower frequency signal also connects these two shelf regions.
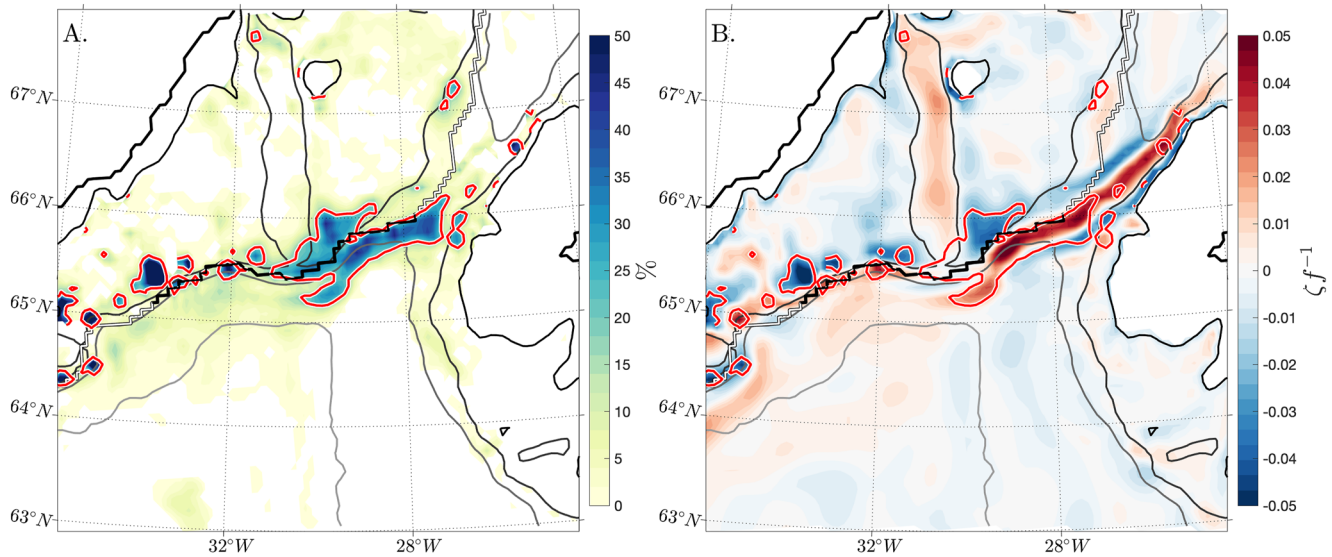
Figure 10. (a) Percent of days in 2005 when the OW parameter indicates the presence of an eddy (OW $< -2\sigma_{OW}$) at 200 m in POP. The red contour surrounds areas where the probability of an eddy being present is >25%. (b) 2005 average nondimensional relative vorticity at 200 m in POP. The red contour from the OW parameter is superimposed. In both panels, contours of the 200, 400, 800, and 2,000 m isobaths are plotted in gray. The along shelf transect is white with the section the DSO eddy region highlighted in black.

3.3. Dynamical Processes Governing Multi-Day Variability

In the Hovmöller diagrams (Figures 8 and 9), we observed high-frequency signals that emanated from a location south of the Denmark Strait. We now explore whether these signals are consistent with the presence of DSO eddies.

We start by using the phase information in the previous subsection to estimate the phase speed of the propagating signal (Münchow et al., 2020; Pickart & Watts, 1990). A middle frequency of each band of coherence was used: $f_{POP} = 0.21$ days^{-1} for POP and $f_{HYCOM} = 0.34$ days^{-1} for HYCOM. A location was chosen along the transect near where the coherence at that frequency is no longer significant: 499 km south of the Denmark Strait in POP, 271 km in HYCOM; the distance between the two locations is D. At that frequency and location, the phase is $\Theta_{XY} = 80°$ in POP and $\Theta_{XY} = 34°$ in HYCOM. We calculate the phase speed as $c_p = f(360/\Theta_{XY})(D/\cos\Delta)$, where Δ is the angle between the wavenumber vector and the direction of the shelf break; the estimate of Δ is the greatest source of uncertainty in this estimate. For POP, the resulting phase velocity is $c_p = 4.5$ m/s and wavelength $\lambda = 1,796$ km while, for HYCOM, the resulting phase velocity is $c_p = 5.2$ m/s and wavelength $\lambda = 1,334$ km. The spectra, coherence, and phase used for estimating the phase velocity are shown in Figure S5 in Supporting Information S1. These phase velocities differ greatly, ~10 times greater than the speed associated with the lines on the Hovmöller diagrams in Figures 8b and 9b.

Phase speed alone is not sufficient to differentiate between TRWs and DSO eddies (Spall & Price, 1998). Coherent eddies can be identified by their high relative vorticity, a measure of the local rotation of a water parcel. A comparison of the magnitude of strain and relative vorticity in a flow, the Okubo–Weiss (OW) parameter, is widely used to track coherent eddies (Okubo, 1970; Weiss, 1991). When vorticity dominates, the OW parameter is negative indicating an eddy is present. We use threshold OW $< -2\sigma_{OW}$ to identify the presence of an eddy, where σ_{OW} is the time-varying spatial average of OW. The percent of days when an eddy was present between 2005 and 2009 at 200 m in POP is plotted in Figure 10a with a red contour showing where the percent of days is >25%. In POP, for the area where the signal is strongest, we calculated the relative vorticity, $\zeta = \partial v/\partial x - \partial u/\partial y$, where u is the zonal velocity and v is the meridional velocity and divide by the Coriolis parameter, f, to define the nondimensional relative vorticity. The average ζf^{-1} at 200 m is plotted in Figure 10b.

Along the shelf break, at 200 m ζf^{-1} is positive (indicating cyclones) off the shelf, and negative (indicating anti-cyclones) on the shelf, consistent with Almansi et al. (2020). The area of strong positive ζf^{-1} is also consistent with the area where eddies are frequently detected with the OW parameter. Combined with the location, the

frequency, the propagation speed along the shelf break, and the spatial pattern of the average nondimensional relative vorticity, we conclude that the high frequency variability in the heat flux across the shelf break is associated with the DSO eddies. In POP, the region where the high frequency signal is observed extends farther along the shelf than the region typically associated with DSO eddies; it is possible that the DSO eddies are generating TRWs in this simulation, but this mechanism has not been explored.

3.4. Impacts of Multi-Day Variability on Net Heat Transport

The high-frequency signals in the Hovmöller diagrams (Figures 10a and 9a) originating to the south of the Denmark Strait are comparable to the topographically trapped Rossby waves (Münchow et al., 2020) in a trough near the Fram Strait, to the cyclonic eddies formed at the Denmark Strait (Moritz et al., 2019), and to the coastally trapped shelf waves in this region (Gelderloos et al., 2021). In the previous section, we found these high-frequency signals to be consistent with DSO eddies traveling along the shelf break. In this section, we want to understand if the multi-day variability impacts cross-shelf heat exchange. We find that on average there is net on-shelf heat flux in POP and off-shelf heat flux in HYCOM, in the region where the eddies are present.

Using Equation 3, we can decompose the heat flux across the isobath into the total, mean, and eddy components. In this context, the "eddy" portion is the contribution to the total heat flux from processes with time scales between 2 and 30 days. In POP, the 2005–2009 average total heat flux onto the shelf in the DSO eddy region, from 102 to 499 km south of the Denmark Strait, is 58 ± 14 PW. This is compared to 46 ± 13 PW of total heat flux across the entire Wide Shelf region in POP. The eddy component of the heat flux in the DSO eddy region is 29 ± 6 PW and 39 ± 10 PW in the entire Wide Shelf; which corresponds to 51% and 85% of the total heat flux in both regions. In POP along the Wide Shelf the eddy component of the heat flux is significant and brings heat onto the shelf. This indicates that these high-frequency signals are an important component of the heat budget in this region.

In HYCOM, the 2005–2009 average total heat flux onto the shelf in the DSO eddy region, from 154 to 271 km south of the Denmark Strait, is -19 PW. Over the entire wide shelf region the total heat flux is onto the shelf, 8.3 PW. The eddy contribution to the heat flux in the DSO eddy region is -2.5 PW which is just 13% of the total off shelf heat flux in that region. Along the entire Wide Shelf, the eddy heat flux is -8.0 PW, which opposes the mean heat flux and is similar in magnitude to the total heat flux onto the shelf. The DSO eddy signal is weaker in HYCOM and manifests itself in a smaller section of the shelf, which could be one reason the eddies do not result in the same contribution to cross-shelf heat flux as seen in POP.

The greater contribution of the mean flow to the total heat flux in HYCOM along the Wide Shelf region is consistent with the differences in surface speed and EKE (Figures 4c and 4f). Along the Southeast shelf, the core of the EGC along the shelf break is stronger and less variable in HYCOM compared to POP. The high EKE region that corresponds to DSO eddy region is much stronger in POP, consistent with the eddies and associated impact on the heat flux being greater. Overall, on shelf heat fluxes in HYCOM along the Wide Shelf are associated with the mean flow, and in POP on shelf heat fluxes are the result the eddying flow.

Because there is a warm bias in the Wide Shelf temperature in POP, and a cold bias in HYCOM, it is possible that the POP simulation is over-representing the heat flux from the DSO eddies, and this process is being under-represented in HYCOM. These simulations do not have the resolution needed to fully resolve mesoscale eddies, and the role that these eddies play in cross-shelf heat flux may be clarified as they are better resolved. Advances in high-resolution modeling have shown that resolving these small-scale processes is important for understanding cross-shelf fluxes (Pennelly et al., 2019; Pennelly & Myers, 2020).

4. Conclusion

In order to assess the heat flux onto the Greenland Continental Shelf, we compared two eddy-permitting coupled ocean-sea ice simulations that employed different ocean components and atmospheric forcing. Using a continental shelf control volume subdivided into three regions, we determine not only how much heat crosses onto the shelf but also the patterns of transport on the shelf. The region of greatest heat flux onto the shelf is between the Denmark Strait and the Sermilik Troughs in southeast Greenland, where the average heat flux is 16.4 ± 13.8 TW in POP and 55.0 ± 23.3 TW in HYCOM. Currents on the shelf are important in spreading warm water to different

shelf regions; in both models the primary source of heat on the southwest continental shelf is from southward flux through the Cape Farewell Gate.

South of the Denmark Strait in both simulations we find a propagating signal in the vertically integrated heat flux with a periods of 3–7 days. This signal contributes to the on-shelf heat flux in this region in POP and the off-shelf heat flux in HYCOM. The location and frequency are consistent with DSO eddies. The section of the shelf along which the heat flux is most impacted is consistent with the portion of the shelf where DSO eddies have been found in previous modeling studies. Further study of the formation of DSO eddies in these simulations is needed. The horizontal resolutions of both the 1/10° and 1/12° simulations limit the representation of mesoscale eddies. The difference in the strength and period of the eddies could be the result of the many differences in model configuration, such as: atmospheric forcing, bathymetry, or the vertical coordinate systems. This study cannot fully separate those differences, but emphasizes the need for continued model intercomparison. The cross-shelf heat flux is just one component of the volume budget for the continental shelf. We find the shelf is too cold in HYCOM and too warm in POP compared to observations from the MEOP program. Further study using higher resolution simulations that could better resolve the dynamics on the shelf could address the bias in on-shelf heat content.

One aspect of the dynamics of the Greenland continental shelf that has been neglected in this study is the role of ice sheet meltwater in these cross-shelf exchange mechanisms. Neither simulation includes a representation of GIS meltwater, which has implications for heat fluxes onto the shelf, as was explored by Gillard et al. (2020). The addition of meltwater from the ice sheet has been shown to strengthen currents and increase heat content on the West Greenland shelf within Baffin Bay (Castro de la Guardia et al., 2015; Grivault et al., 2017). Further simulations are needed to explore the implications of accelerated melting on shelf warming. In addition, our study has shown that mesoscale processes contribute to on-shelf heat flux. High-resolution studies that resolve mesoscale (and finer) processes and features in this region are needed to better understand these processes. Such high-resolution studies could also address the dynamics between the shelf break and the ice sheets that bring the warm water we observe crossing the shelf to the front of glaciers where it drives melting.

Data Availability Statement

Selected output from the POP and HYCOM simulations used in this paper are publicly available through the UC San Diego Library Digital Collections https://doi.org/10.6075/J0319W2S.

References

Almansi, M., Haine, T., Gelderloos, R., & Pickart, R. (2020). Evolution of Denmark Strait overflow cyclones and their relationship to overflow surges. *Geophysical Research Letters*, *47*(4), e2019GL086759. https://doi.org/10.1029/2019gl086759

Almansi, M., Haine, T. W., Pickart, R. S., Magaldi, M. G., Gelderloos, R., & Mastropole, D. (2017). High-frequency variability in the circulation and hydrography of the Denmark Strait overflow from a high-resolution numerical model. *Journal of Physical Oceanography*, *47*(12), 2999–3013. https://doi.org/10.1175/jpo-d-17-0129.1

Appen, W.-J. v., Mastropole, D., Pickart, R. S., Valdimarsson, H., Jónsson, S., & Girton, J. B. (2017). On the nature of the mesoscale variability in Denmark Strait. *Journal of Physical Oceanography*, *47*(3), 567–582. https://doi.org/10.1175/jpo-d-16-0127.1

Appen, W.-J. v., Pickart, R. S., Brink, K. H., & Haine, T. W. (2014). Water column structure and statistics of Denmark Strait overflow water cyclones. *Deep Sea Research Part I: Oceanographic Research Papers*, *84*, 110–126. https://doi.org/10.1016/j.dsr.2013.10.007

Arzeno-Soltero, I. B., Giddings, S. N., Pawlak, G., McClean, J. L., Wang, H., Rainville, L., & Lee, C. M. (2021). Generation of low-latitude seamount-trapped waves: A case study of the Seychelles plateau. *Journal of Geophysical Research: Oceans*, *126*(8), e2021JC017234. https://doi.org/10.1029/2021JC017234

Bacon, S., & Fofonoff, N. (1996). Oceanic heat flux calculation. *Journal of Atmospheric and Oceanic Technology*, *13*(6), 1327–1329. https://doi.org/10.1175/1520-0426(1996)013<1327:ohfc>2.0.co;2;2

Bacon, S., Marshall, A., Holliday, N. P., Aksenov, Y., & Dye, S. R. (2014). Seasonal variability of the East Greenland coastal current. *Journal of Geophysical Research: Oceans*, *119*(6), 3967–3987. https://doi.org/10.1002/2013jc009279

Benn, D. I., Cowton, T., Todd, J., & Luckman, A. (2017). Glacier calving in Greenland. *Current Climate Change Reports*, 3(4), 282–290. https://doi.org/10.1007/s40641-017-0070-1

Bleck, R. (2002). An oceanic general circulation model framed in hybrid isopycnic-Cartesian coordinates. *Ocean Modelling*, 4(1), 55–88. https://doi.org/10.1016/s1463-5003(01)00012-9

Böning, C. W., Behrens, E., Biastoch, A., Getzlaff, K., & Bamber, J. L. (2016). Emerging impact of Greenland meltwater on deepwater formation in the North Atlantic Ocean. *Nature Geoscience*, *9*(7), 523–527. https://doi.org/10.1038/ngeo2740

Brandt, P., Schott, F. A., Funk, A., & Martins, C. S. (2004). Seasonal to interannual variability of the eddy field in the Labrador Sea from satellite altimetry. *Journal of Geophysical Research*, *109*(C2), C02028. https://doi.org/10.1029/2002jc001551

Carnes, M. R., Helber, R. W., Barron, C. N., & Dastugue, J. M. (2010). *Validation test report for GDEM4 (Tech. Rep.)*. Naval Research Lab Stennis Space Center MS Oceanography Div.

Castillo-Trujillo, A. C., Arzeno-Soltero, I. B., Giddings, S. N., Pawlak, G., McClean, J., & Rainville, L. (2021). Observations and modeling of ocean circulation in the Seychelles Plateau Region. *Journal of Geophysical Research: Oceans*, *126*(2), e2020JC016593. https://doi.org/10.1029/2020JC016593

Castro de la Guardia, L., Hu, X., & Myers, P. G. (2015). Potential positive feedback between Greenland ice sheet melt and Baffin Bay heat content on the west Greenland shelf. *Geophysical Research Letters*, *42*(12), 4922–4930. https://doi.org/10.1002/2015gl064626

Chassignet, E. P., Hurlburt, H. E., Metzger, E. J., Smedstad, O. M., Cummings, J., Halliwell, G. R., et al. (2009). Global ocean prediction with the HYbrid coordinate Ocean Model (HYCOM). *Oceanography*, *22*(2), 64–75. https://doi.org/10.5670/oceanog.2009.39

Chassignet, E. P., Hurlburt, H. E., Smedstad, O. M., Halliwell, G. R., Hogan, P. J., Wallcraft, A. J., et al. (2007). The HYCOM (HYbrid Coordinate Ocean Model) data assimilative system. *Journal of Marine Systems*, *65*(1–4), 60–83. https://doi.org/10.1016/j.jmarsys.2005.09.016

Chassignet, E. P., Smith, L. T., Halliwell, G. R., & Bleck, R. (2003). North atlantic simulations with the HYbrid Coordinate Ocean Model (HYCOM): Impact of the vertical coordinate choice, reference density, and thermobaricity. *Journal of Physical Oceanography*, *33*(12), 2504–2526. https://doi.org/10.1175/1520-0485(2003)033<2504:naswth>2.0.co;2

Christoffersen, P., Mugford, R., Heywood, K., Joughin, I., Dowdeswell, J., Syvitski, J., et al. (2011). Warming of waters in an east Greenland fjord prior to glacier retreat: Mechanisms and connection to large-scale atmospheric conditions. *The Cryosphere*, *5*(3), 701–714. https://doi.org/10.5194/tc-5-701-2011

Christoffersen, P., O'Leary, M., Van Angelen, J. H., & Van Den Broeke, M. (2012). Partitioning effects from ocean and atmosphere on the calving stability of Kangerdlugssuaq Glacier, East Greenland. *Annals of Glaciology*, *53*(60), 249–256. https://doi.org/10.3189/2012aog60a087

Curry, B., Lee, C. M., Petrie, B., Moritz, R. E., & Kwok, R. (2014). Multiyear volume, liquid freshwater, and sea ice transports through Davis Strait, 2004–10. *Journal of Physical Oceanography*, *44*(4), 1244–1266. https://doi.org/10.1175/jpo-d-13-0177.1

Dukhovskoy, D. S., Chassignet, E. P., Hogan, P. J., Metzger, E. J., Posey, P., Smedstad, O. M., et al. (2016). Current state and recent changes in the Arctic Ocean from the HYCOM-NCODA global ocean and sea ice prediction system. *Agu Fall Meeting Abstracts*, *2016*, GC23H–07.

Dukhovskoy, D. S., Yashayaev, I., Chassignet, E. P., Meyers, P. G., Platov, G., & Proshutinsky, A. (2021). Time scales of the Greenland freshwater anomaly in the subpolar North Atlantic. *Journal of Climate*, 1–58. https://doi.org/10.1175/jcli-d-20-0610.1

Dukhovskoy, D. S., Yashayaev, I., Proshutinsky, A., Bamber, J., Bashmachnikov, I., Chassignet, E., et al. (2019). Role of Greenland freshwater anomaly in the recent freshening of the subpolar North Atlantic. *Journal of Geophysical Research: Oceans*, *124*(5), 3333–3360. https://doi.org/10.1029/2018jc014686

Dukowicz, J. K., & Smith, R. D. (1994). Implicit free-surface method for the Bryan-Cox-Semtner ocean model. *Journal of Geophysical Research*, *99*(C4), 7991–8014. https://doi.org/10.1029/93jc03455

Foukal, N. P., Gelderloos, R., & Pickart, R. S. (2020). A continuous pathway for fresh water along the East Greenland shelf. *Science Advances*, *6*(43), eabc4254. https://doi.org/10.1126/sciadv.abc4254

Fraser, N. J., & Inall, M. E. (2018). Influence of barrier wind forcing on heat delivery toward the Greenland Ice Sheet. *Journal of Geophysical Research: Oceans*, *123*(4), 2513–2538. https://doi.org/10.1002/2017jc013464

Fratantoni, D. M. (2001). North Atlantic surface circulation during the 1990s observed with satellite-tracked drifters. *Journal of Geophysical Research*, *106*(C10), 22067–22093. https://doi.org/10.1029/2000jc000730

Furevik, T., & Nilsen, J. E. Ø. (2005). Large-scale atmospheric circulation variability and its impacts on the Nordic seas ocean climate—A review. In *The Nordic seas: An integrated perspective* (pp. 105–136). American Geophysical Union (AGU). https://doi.org/10.1029/158GM09

Gelderloos, R., Haine, T. W., & Almansi, M. (2021). Coastal trapped waves and other subinertial variability along the Southeast Greenland Coast in a realistic numerical simulation. *Journal of Physical Oceanography*, *51*(3), 861–877. https://doi.org/10.1175/jpo-d-20-0239.1

Gelderloos, R., Haine, T. W., Koszalka, I. M., & Magaldi, M. G. (2017). Seasonal variability in warm-water inflow toward Kangerdlugssuaq Fjord. *Journal of Physical Oceanography*, *47*(7), 1685–1699. https://doi.org/10.1175/jpo-d-16-0202.1

Gillard, L. C., Hu, X., Myers, P. G., Ribergaard, M. H., & Lee, C. M. (2020). Drivers for Atlantic-origin waters abutting Greenland. *The Cryosphere*, *14*(8), 2729–2753. https://doi.org/10.5194/tc-14-2729-2020

Gouretski, V., & Koltermann, K. P. (2004). WOCE global hydrographic climatology. *Berichte des BSH*, *35*, 1–52.

Grist, J. P., Josey, S. A., Boehme, L., Meredith, M. P., Laidre, K. L., Heide-Jørgensen, M. P., et al. (2014). Seasonal variability of the warm Atlantic water layer in the vicinity of the Greenland shelf break. *Geophysical Research Letters*, *41*(23), 8530–8537. https://doi.org/10.1002/2014gl062051

Grivault, N., Hu, X., & Myers, P. G. (2017). Evolution of Baffin Bay water masses and transports in a numerical sensitivity experiment under enhanced Greenland Melt. *Atmosphere-Ocean*, *55*(3), 169–194. https://doi.org/10.1080/07055900.2017.1333950

Hallberg, R. (2013). Using a resolution function to regulate parameterizations of oceanic mesoscale eddy effects. *Ocean Modelling*, *72*, 92–103. https://doi.org/10.1016/j.ocemod.2013.08.007

Hanna, E., Jones, J. M., Cappelen, J., Mernild, S. H., Wood, L., Steffen, K., & Huybrechts, P. (2013). The influence of North Atlantic atmospheric and oceanic forcing effects on 1900–2010 Greenland summer climate and ice melt/runoff. *International Journal of Climatology*, *33*(4), 862–880. https://doi.org/10.1002/joc.3475

Håvik, L., Våge, K., Pickart, R. S., Harden, B., Appen, W.-J. v., Jónsson, S., & Østerhus, S. (2017). Structure and variability of the shelfbreak east Greenland current north of Denmark Strait. *Journal of Physical Oceanography*, *47*(10), 2631–2646. https://doi.org/10.1175/jpo-d-17-0062.1

Holland, D. M., Thomas, R. H., De Young, B., Ribergaard, M. H., & Lyberth, B. (2008). Acceleration of Jakobshavn Isbrae triggered by warm subsurface ocean waters. *Nature Geoscience*, *1*(10), 659–664. https://doi.org/10.1038/ngeo316

Holliday, N. P., Bacon, S., Cunningham, S. A., Gary, S. F., Karstensen, J., King, B. A., et al. (2018). Subpolar North Atlantic overturning and gyre-scale circulation in the summers of 2014 and 2016. *Journal of Geophysical Research: Oceans*, *123*(7), 4538–4559. https://doi.org/10.1029/2018jc013841

Howat, I. M., Smith, B. E., Joughin, I., & Scambos, T. A. (2008). Rates of southeast Greenland ice volume loss from combined ICESat and ASTER observations. *Geophysical Research Letters*, *35*(17), L17505. https://doi.org/10.1029/2008gl034496

Hunke, E. C., Lipscomb, W. H., Turner, A. K., Jeffery, N., & Elliott, S. (2010). *Cice: The Los Alamos sea ice model documentation and software user's manual version 4.1 LA-CC-06-012. T-3 fluid dynamics group*. Los Alamos National Laboratory.675.

Hurrell, J. W., Holland, M. M., Gent, P. R., Ghan, S., Kay, J. E., Kushner, P. J., et al. (2013). The community Earth system model: A framework for collaborative research. *Bulletin of the American Meteorological Society*, *94*(9), 1339–1360. https://doi.org/10.1175/bams-d-12-00121.1

Jackson, R. H., Lentz, S. J., & Straneo, F. (2018). The dynamics of shelf forcing in Greenlandic fjords. *Journal of Physical Oceanography*, *48*(11), 2799–2827. https://doi.org/10.1175/jpo-d-18-0057.1

Jackson, R. H., Straneo, F., & Sutherland, D. A. (2014). Externally forced fluctuations in ocean temperature at Greenland glaciers in non-summer months. *Nature Geoscience*, *7*(7), 503–508. https://doi.org/10.1038/ngeo2186

Large, W. G., & Yeager, S. (2009). The global climatology of an interannually varying air–sea flux data set. *Climate Dynamics*, *33*(2–3), 341–364. https://doi.org/10.1007/s00382-008-0441-3

Laurindo, L. C., Mariano, A. J., & Lumpkin, R. (2017). An improved near-surface velocity climatology for the global ocean from drifter observations. *Deep Sea Research Part I: Oceanographic Research Papers*, *124*, 73–92. https://doi.org/10.1016/j.dsr.2017.04.009

Le Bras, I. A.-A., Straneo, F., Holte, J., & Holliday, N. P. (2018). Seasonality of freshwater in the east Greenland current system from 2014 to 2016. *Journal of Geophysical Research: Oceans*, *123*(12), 8828–8848. https://doi.org/10.1029/2018jc014511

Luthcke, S. B., Zwally, H. J., Abdalati, W., Rowlands, D. D., Ray, R. D., Nerem, R. S., et al. (2006). Recent Greenland ice mass loss by drainage system from satellite gravity observations. *Science*, *314*(5803), 1286–1289. https://doi.org/10.1126/science.1130776

McClean, J. L., Bader, D. C., Bryan, F. O., Maltrud, M. E., Dennis, J. M., Mirin, A. A., et al. (2011). A prototype two-decade fully-coupled fine-resolution CCSM simulation. *Ocean Modelling*, *39*(1–2), 10–30. https://doi.org/10.1016/j.ocemod.2011.02.011

McClean, J. L., Bader, D. C., Maltrud, M. E., Evans, K. J., Taylor, M., Tang, Q., & Mahajan, S. (2018). High-resolution fully-coupled ACME v0.1 approximate present day transient climate simulations. *Ocean Sciences Meeting 2018, 12-16/February, Portland/OR. Abstract ID: OM44C-2143*.

Meehl, G. A., Stocker, T. F., Collins, W. D., Friedlingstein, P., Gaye, T., Gregory, J. M., et al. (Eds.). In Climate change 2007: The physical science basis. Contribution of Working Group I to the Fourth Assessment report of the Intergovernmental panel on climate change. Cambridge University Press.

Metzger, E. J., Smedstad, O. M., Thoppil, P. G., Hurlburt, H. E., Cummings, J. A., Wallcraft, A. J., et al. (2014). US Navy operational global ocean and Arctic ice prediction systems. *Oceanography*, *27*(3), 32–43. https://doi.org/10.5670/oceanog.2014.66

Millan, R., Rignot, E., Mouginot, J., Wood, M., Bjørk, A. A., & Morlighem, M. (2018). Vulnerability of southeast Greenland glaciers to warm Atlantic water from operation IceBridge and ocean melting Greenland data. *Geophysical Research Letters*, *45*(6), 2688–2696. https://doi.org/10.1002/2017gl076561

Moritz, M., Jochumsen, K., North, R. P., Quadfasel, D., & Valdimarsson, H. (2019). Mesoscale eddies observed at the Denmark Strait sill. *Journal of Geophysical Research: Oceans*, *124*(11), 7947–7961. https://doi.org/10.1029/2019jc015273

Mouginot, J., Rignot, E., Bjørk, A. A., Van den Broeke, M., Millan, R., Morlighem, M., et al. (2019). Forty-six years of Greenland Ice Sheet mass balance from 1972 to 2018. *Proceedings of the National Academy of Sciences*, *116*(19), 201904242–201909244. https://doi.org/10.1073/pnas.1904242116

Münchow, A., Schaffer, J., & Kanzow, T. (2020). Ocean circulation connecting Fram Strait to glaciers off Northeast Greenland: Mean flows, topographic Rossby waves, and their forcing. *Journal of Physical Oceanography*, *50*(2), 509–530. https://doi.org/10.1175/jpo-d-19-0085.1

Murray, R. J. (1996). Explicit generation of orthogonal grids for ocean models. *Journal of Computational Physics*, *126*(2), 251–273. https://doi.org/10.1006/jcph.1996.0136

Myers, P. G., Donnelly, C., & Ribergaard, M. H. (2009). Structure and variability of the West Greenland Current in summer derived from 6 repeat standard sections. *Progress in Oceanography*, *80*(1–2), 93–112. https://doi.org/10.1016/j.pocean.2008.12.003

Nurser, A., & Bacon, S. (2014). The Rossby radius in the Arctic Ocean. *Ocean Science*, *10*(6), 967–975. https://doi.org/10.5194/os-10-967-2014

Okubo, A. (1970). Horizontal dispersion of floatable particles in the vicinity of velocity singularities such as convergences. *Deep Sea Research and Oceanographic Abstracts*, *17*(3), 445–454. https://doi.org/10.1016/0011-7471(70)90059-8

Østerhus, S., Woodgate, R., Valdimarsson, H., Turrell, B., De Steur, L., Quadfasel, D., et al. (2019). Arctic Mediterranean exchanges: A consistent volume budget and trends in transports from two decades of observations. *Ocean Science*, *15*(2), 379–399. https://doi.org/10.5194/os-15-379-2019

Palóczy, A., Gille, S. T., & McClean, J. L. (2018). Oceanic heat delivery to the Antarctic Continental Shelf: Large-scale, low-frequency variability. *Journal of Geophysical Research: Oceans*, *123*(11), 7678–7701. https://doi.org/10.1029/2018jc014345

Palóczy, A., McClean, J. L., Gille, S. T., & Wang, H. (2020). The large-scale vorticity balance of the Antarctic continental margin in a fine-resolution global simulation. *Journal of Physical Oceanography*, *50*(8), 2173–2188. https://doi.org/10.1175/jpo-d-19-0307.1

Pennelly, C., Hu, X., & Myers, P. G. (2019). Cross-isobath freshwater exchange within the North Atlantic subpolar gyre. *Journal of Geophysical Research: Oceans*, *124*(10), 6831–6853. https://doi.org/10.1029/2019jc015144

Pennelly, C., & Myers, P. G. (2020). Introducing LAB60: A 1/60°NEMO 3.6 numerical simulation of the Labrador Sea. *Geoscientific Model Development*, *13*(10), 4959–4975. https://doi.org/10.5194/gmd-13-4959-2020

Pickart, R. S., & Watts, D. R. (1990). Deep Western boundary current variability at Cape Hatteras. *Journal of Marine Research*, *48*(4), 765–791. https://doi.org/10.1357/002224090784988674

Rignot, E., Fenty, I., Menemenlis, D., & Xu, Y. (2012). Spreading of warm ocean waters around Greenland as a possible cause for glacier acceleration. *Annals of Glaciology*, *53*(60), 257–266. https://doi.org/10.3189/2012aog60a136

Rossby, T., Flagg, C., Chafik, L., Harden, B., & Søiland, H. (2018). A direct estimate of volume, heat, and freshwater exchange across the Greenland-Iceland-Faroe-Scotland Ridge. *Journal of Geophysical Research: Oceans*, *123*(10), 7139–7153. https://doi.org/10.1029/2018jc014250

Saha, S., Moorthi, S., Pan, H.-L., Wu, X., Wang, J., Nadiga, S., et al. (2010). The NCEP climate forecast system reanalysis. *Bulletin of the American Meteorological Society*, *91*(8), 1015–1058. https://doi.org/10.1175/2010bams3001.1

Saha, S., Moorthi, S., Wu, X., Wang, J., Nadiga, S., Tripp, P., et al. (2014). The NCEP climate forecast system version 2. *Journal of Climate*, *27*(6), 2185–2208. https://doi.org/10.1175/jcli-d-12-00823.1

Saini, J., Stein, R., Fahl, K., Weiser, J., Hebbeln, D., Hillaire-Marcel, C., & De Vernal, A. (2020). Holocene variability in sea ice and primary productivity in the northeastern Baffin Bay. *Arktos*, *6*(1), 55–73. https://doi.org/10.1007/s41063-020-00075-y

Schauer, U., & Beszczynska-Möller, A. (2009). Problems with estimation and interpretation of oceanic heat transport–conceptual remarks for the case of Fram Strait in the Arctic Ocean. *Ocean Science*, *5*(4), 487–494. https://doi.org/10.5194/os-5-487-2009

Schulze Chretien, L. M., & Frajka-Williams, E. (2018). Wind-driven transport of fresh shelf water into the upper 30 m of the Labrador Sea. *Ocean Science*, *14*(5), 1247–1264. https://doi.org/10.5194/os-14-1247-2018

Smith, B., Fricker, H. A., Gardner, A. S., Medley, B., Nilsson, J., Paolo, F. S., et al. (2020). Pervasive ice sheet mass loss reflects competing ocean and atmosphere processes. *Science*, *368*(6496), 1239–1242. https://doi.org/10.1126/science.aaz5845

Smith, R., & Gent, P. (2002). Reference manual for the Parallel Ocean Program (POP). Los Alamos unclassified report LA-UR-02-2484.

Spall, M. A., & Price, J. F. (1998). Mesoscale variability in Denmark Strait: The PV outflow hypothesis. *Journal of Physical Oceanography*, *28*(8), 1598–1623. https://doi.org/10.1175/1520-0485(1998)028<1598:mvidst>2.0.co;2

Straneo, F., & Cenedese, C. (2015). The dynamics of Greenland's glacial fjords and their role in climate. *Annual Review of Marine Science*, *7*(1), 89–112. https://doi.org/10.1146/annurev-marine-010213-135133

Straneo, F., & Heimbach, P. (2013). North Atlantic warming and the retreat of Greenland's outlet glaciers. *Nature*, *504*(7478), 36–43. https://doi.org/10.1038/nature12854

Straneo, F., Heimbach, P., Sergienko, O., Hamilton, G., Catania, G., Griffies, S., et al. (2013). Challenges to understanding the dynamic response of Greenland's marine terminating glaciers to oceanic and atmospheric forcing. *Bulletin of the American Meteorological Society*, *94*(8), 1131–1144. https://doi.org/10.1175/bams-d-12-00100.1

Straneo, F., Sutherland, D. A., Holland, D., Gladish, C., Hamilton, G. S., Johnson, H. L., et al. (2012). Characteristics of ocean waters reaching Greenland's glaciers. *Annals of Glaciology*, *53*(60), 202–210. https://doi.org/10.3189/2012aog60a059

Sutherland, D. A., & Pickart, R. S. (2008). The East Greenland coastal current: Structure, variability, and forcing. *Progress in Oceanography*, *78*(1), 58–77. https://doi.org/10.1016/j.pocean.2007.09.006

Sutherland, D. A., Straneo, F., Stenson, G. B., Davidson, F. J., Hammill, M. O., & Rosing-Asvid, A. (2013). Atlantic water variability on the SE Greenland continental shelf and its relationship to SST and bathymetry. *Journal of Geophysical Research: Oceans*, *118*(2), 847–855. https://doi.org/10.1029/2012jc008354

Treasure, A. M., Roquet, F., Ansorge, I. J., Bester, M. N., Boehme, L., Bornemann, H., et al. (2017). Marine mammals exploring the Oceans pole to pole: A review of the MEOP consortium. *Oceanography*, *30*(2), 132–138. https://doi.org/10.5670/oceanog.2017.234

Trodahl, M., & Isachsen, P. E. (2018). Topographic influence on baroclinic instability and the mesoscale eddy field in the northern North Atlantic Ocean and the Nordic Seas. *Journal of Physical Oceanography*, *48*(11), 2593–2607. https://doi.org/10.1175/jpo-d-17-0220.1

Van den Broeke, M., Bamber, J., Ettema, J., Rignot, E., Schrama, E., Van de Berg, W. J., et al. (2009). Partitioning recent Greenland mass loss. *Science*, *326*(5955), 984–986. https://doi.org/10.1126/science.1178176

Wang, H., McClean, J. L., & Talley, L. D. (2021). Full vorticity budget of the Arabian Sea from a 0.1 ocean model: Sverdrup dynamics, Rossby waves, and nonlinear eddy effects. *Journal of Physical Oceanography*, *51*(12), 3589–3607. https://doi.org/10.1175/jpo-d-20-0223.1

Wang, H., McClean, J. L., Talley, L. D., & Yeager, S. (2018). Seasonal cycle and annual reversal of the Somali Current in an eddy-resolving global ocean model. *Journal of Geophysical Research: Oceans*, *123*(9), 6562–6580. https://doi.org/10.1029/2018jc013975

Weiss, J. (1991). The dynamics of ensotrophy transfer in two-dimensional hydrodynamics. *Physica D: Nonlinear Phenomena*, *48*(2–3), 273–294. https://doi.org/10.1016/0167-2789(91)90088-q

Wouters, B., Chambers, D., & Schrama, E. J. O. (2008). GRACE observes small-scale mass loss in Greenland. *Geophysical Research Letters*, *35*(20), L20501. https://doi.org/10.1029/2008GL034816